Bedrock fracture density controls on hillslope erodibility in steep, rocky landscapes with patchy soil cover, southern California, USA

Alexander B. Neely[1], Roman A. DiBiase[1, 2], Lee B. Corbett[3], Paul R. Bierman[3], Marc W. Caffee[4,5]

[1]*Department of Geosciences, Pennsylvania State University, University Park, Pennsylvania, USA 16802*

[2]*Earth and Environmental Systems Institute, Pennsylvania State University, University Park, Pennsylvania, USA 16802*

[3]*Department of Geology, University of Vermont, Burlington, Vermont, USA 05405*

[4]*Department of Physics and Astronomy, Purdue University, West Lafayette, Indiana, USA 47907*

[5]*Department of Earth, Atmospheric, and Planetary Sciences, Purdue University, West Lafayette, Indiana, USA 47907*

Corresponding Author Contact Information: abn5031@psu.edu

Abstract

Although many steep landscapes comprise a patchwork of soil-mantled and bare-bedrock hillslopes, models typically assume hillslopes are entirely soil-mantled or bare-bedrock, making it challenging to predict how rock properties influence hillslope erodibility and landscape evolution. Here, we study headwater catchments across the San Gabriel Mountains (SGM) and Northern San Jacinto Mountains (NSJM) in southern California; two steep landscapes with similar climate and lithology, but with distinctly different bedrock fracture densities, ~5× higher in the SGM. We combine new and published detrital in-situ cosmogenic ^{10}Be-derived erosion rates with analysis of high resolution imagery and topography to quantify how the morphology and abundance of bare-bedrock and soil-mantled hillslopes vary with erosion rate within and between the two landscapes. For similar mean hillslope angles (35-46°), catchments in the NSJM erode at rates of 0.1-0.6 m kyr^{-1}, compared to 0.2-2.2 m kyr^{-1} in the SGM. In both landscapes, bare-bedrock hillslopes increase in abundance with increasing erosion rate; however, more and

steeper bedrock is exposed in the NSJM, indicating that wider bedrock fracture spacing reduces soil production efficiency and supports steeper cliffs. Additionally, higher erosion rates in the SGM require a 3× higher soil transport efficiency, reflecting an indirect control of bedrock fracture density on the size of sediment armoring hillslopes. Our data highlight how hillslope morphodynamics in steep landscapes depend on the strength of soil and bedrock and the efficiency of soil production and transport, all of which are variably sensitive to rock properties and influence the partitioning of soil and bare-bedrock on hillslopes.

1. Introduction

The presence or absence of soil on hillslopes exerts a major influence on the structure and function of Earth's critical zone, with implications for hydrology, ecology, landscape evolution, and natural hazards. Soil supports terrestrial ecosystems (Graham et al., 2010), influences river function by reducing the grain size of sediment delivered to channel networks (Sklar et al., 2017), and facilitates climate-modulating silicate weathering feedbacks (Dixon and Von Blanckenburg, 2012). In landscapes where soil cover is discontinuous or absent on hillslopes, bedrock cliffs, steeper topography, sparser vegetation, and reduced infiltration capacity lead to flashier hydrographs, increasing the potential for hazardous floods and debris flows (Coe et al., 2008).

Steep hillslopes are often characterized by a patchwork of thin soil cover and bare-bedrock outcrops, reflecting a competition between soil production, soil transport, and slope stability thresholds of soil and bedrock that vary in space and time (Carson and Kirkby, 1972; Dietrich et al., 2003). If soil production rates keep pace with hillslope erosion rates, hillslopes remain soil-mantled, and a robust framework exists to describe the relationship between hillslope morphology, soil thickness, and erosion rate (Heimsath et al., 1997; Roering, 2008). However, if hillslope erosion rates locally exceed rates of soil production, bare bedrock is exposed, and no framework exists to describe the morphodynamics of mixed bedrock and soil-mantled hillslopes.

A strength contrast between bedrock and soil may significantly control hillslope morphology in steep landscapes where hillslope angles are near material stability limits (e.g. Schmidt and Montgomery, 1995; Korup, 2008). Whereas variations in the critical slope (angle of repose) for soil stability are straightforward to assess and rarely exceed 45–50° (Roering et al., 1999), the morphology of bare-bedrock hillslopes expresses a more direct connection to rock

material properties (Selby, 1982; Moore et al., 2009) and varies considerably among landscapes, often greatly exceeding the stability thresholds of soil. Despite having implications for understanding rock strength controls on landscape evolution, differences in the relative abundance and effective rock strength of bedrock and soil-mantled hillslopes have not been considered when relating patterns in catchment-mean hillslope morphology to erosion rates.

High resolution imagery and lidar-generated topography resolve the morphology of rugged terrain in detail and provide an opportunity to map, quantify, and compare the morphology of bedrock and soil-mantled hillslopes (e.g. DiBiase et al., 2012; Milodowski et al., 2015). Earlier work in the San Gabriel Mountains, California showed that as catchments steepen and erosion rates increase, a continuous soil mantle is broken by more frequent stochastic landslides that locally strip soil and expose steep, bare-bedrock hillslopes (Heimsath et al., 2012; DiBiase et al., 2012). However, these studies did not analyze how the morphology of bedrock and soil-mantled hillslopes evolve separately, and these studies were limited to a narrow spectrum of climatic and lithologic conditions in the San Gabriel Mountains.

It remains challenging to understand what conditions cause landscapes to transition from fully soil-mantled hillslopes to a patchwork of soil-mantled and bare-bedrock hillslopes. A wide range of soil production rates measured using cosmogenic nuclides show that soil production rates are sensitive to a combination of climatic, lithologic, and tectonic factors (Heimsath et al., 2012). We use the term soil production efficiency to describe the sensitivity of soil production rates to these factors in landscapes with thin or patchy soil cover, and we infer the relative soil production efficiency in a given landscape from the catchment erosion rate above which hillslopes become progressively rockier. For example, in the Southern Alps of New Zealand, high rainfall rates across catchments underlain by fractured metamorphic rock facilitate high soil

production rates, and minimal bare-bedrock exposure is seen on hillslopes despite erosion rates >2 m kyr^{-1}, indicating high soil production efficiency (Larsen et al., 2014). In contrast, patchy soil cover and widespread bedrock exposure on granitic hillslopes in the Sierra Nevada Mountains are thought to reflect the distribution of phosphorous-poor plutonic rocks that limit vegetation growth and soil production. In the Sierra Nevada Mountains, bare-bedrock hillslopes are seen at catchment erosion rates that range from 0.02–0.08 m kyr^{-1} (Granger et al., 2001; Hahm et al., 2014), indicating that some catchments have soil production efficiencies that are 1-2 orders of magnitude lower than that in the Southern Alps, NZ. Comparisons across different study sites and separate analysis of morphodynamics on bare-bedrock and soil-mantled hillslopes are needed to better constrain how climatic, tectonic, and lithologic factors control the relationship between hillslope morphology, bedrock exposure, and erosion rate in steep landscapes.

In this study, we investigate the relationship between hillslope morphology, bedrock exposure, and erosion rate for two steep mountain ranges in southern California underlain by similar granite-dominated lithology but with strongly-contrasting bedrock fracture density. We quantify hillslope erosion rates from new and previously published detrital in-situ cosmogenic ^{10}Be samples taken from steep headwater catchments that have ~0–70% bedrock exposure on hillslopes. We use high-resolution imagery and lidar-derived topography to map the extent and quantify the morphology of soil-mantled and bare-bedrock hillslopes within each catchment. We then use these data to compare the efficiency of soil production and soil transport in both landscapes, and we discuss the implications for how rock material properties influence the relationship between hillslope morphology and erosion rate.

2. Study Area

105 We compare the San Gabriel Mountains and the Northern San Jacinto Mountains, two
106 landscapes in southern California that exhibit broadly similar topographic relief, lithology, and
107 climate but differ in bedrock fracture density and tectonic environment (Fig. 1). The San Gabriel
108 Mountains (SGM) are a tectonically active mountain range located along a restraining bend in
109 the San Andreas Fault, bounded to the south by thrusting along the Sierra Madre-Cucamonga
110 Fault Zone (Crook et al., 1987). The SGM are heavily dissected by Miocene to recent faults, and
111 bedrock cliffs are typically fractured at the decimeter scale (Fig. 2; DiBiase et al., 2012; 2018a).
112 In contrast, the Northern San Jacinto Mountains (NSJM), located in the footwall of the San
113 Gorgonio Pass-Garnet Hill dextral-reverse fault system, are interpreted to be a relatively intact
114 structural block (Yule and Sieh, 2003). The NSJM have fewer mapped faults, and cliffs typically
115 exhibit wide (meter-scale) bedrock fracture spacing (Fig 2; DiBiase et al., 2018a).
116 Bedrock geology, climate, and vegetation cover are similar between the NSJM and SGM,
117 and we analyze headwater catchments that span the topographic and climatic variability within
118 each mountain range. In both landscapes, Cretaceous tonalite and granodiorite are the most
119 abundant rock types, with small enclaves of quartzite, schist, and marble (Jennings et al., 1977).
120 Mean annual temperatures vary spatially between 6–13˚C in the SGM and 4–12˚C in the NSJM
121 (http://prism.oregonstate.edu). There is no evidence of cirques or moraines, suggesting that both
122 mountain ranges were deglaciated throughout the Pleistocene. Rainfall is seasonal in both
123 ranges, and most precipitation occurs between November and April. Mean annual precipitation
124 increases with elevation in each landscape, and is generally higher in the SGM (630–1350 mm
125 yr^{-1}) compared to the NSJM (400–720 mm yr^{-1}) (http://prism.oregonstate.edu). In both
126 landscapes, low elevation chaparral hillslopes are dominated by chamise (*Adenostoma*
127 *fasciculation*) and manzanita (*A. manzanita*), and elevations above 1,500– 2,000 m are generally

dominated by pine forests (*Pinus Jeffereyi, Pineus Lambertina, Pinus Ponderosa*) (Critchfield, 1971). Vegetation in both landscapes is sparse on bedrock cliffs (Fig. 2).

Prior studies exploited a west-east tectonic gradient in the SGM (Blythe et al., 2002; DiBiase et al., 2010) to analyze how soil production and weathering extent vary as a function of increasing physical erosion rate across a region with relatively homogenous climate and rock strength (Dixon et al., 2012; Heimsath et al., 2012). In the SGM, soils directly overlie fractured bedrock and are less weathered where physical erosion rates exceed ~0.1 m kyr^{-1} (Dixon et al., 2012), and the chemical depletion of soils in the SGM is interpreted to vary more strongly with physical erosion rate than with climatic variation. Additionally, soil production rates track catchment erosion rates even in rapidly eroding catchments characterized by thin, patchy soils and incipient bedrock exposure (Heimsath et al., 2012). Thus, measurements of detrital cosmogenic ^{10}Be from headwater catchments serve as a proxy for soil production rates in steep catchments. Although catchment erosion rates measured using cosmogenic ^{10}Be have been quantified across much of the SGM (DiBiase et al., 2010), there are few data from the steepest, rockiest catchments concentrated in the eastern SGM, where we focus our analysis in this study.

In the NSJM, no prior studies directly constrain soil production rates and chemical weathering extent on hillslopes, and there are few existing measurements of catchment erosion rates from cosmogenic ^{10}Be (Rossi, 2014; DiBiase et al., 2018a). Field observations indicate that NSJM soils are thin (<1 m) and patchy, similar to soils in the SGM (Fig. 2). Although the NSJM receive less rainfall than the SGM, we focus on headwater catchments in the NSJM where climate and vegetation cover are most similar to sites in the SGM, in order to isolate rock strength controls on the morphology, bedrock exposure, and erosion rate of steep hillslopes. Thus, we assume that the largest environmental difference between our sites in the NSJM and

SGM is a difference in bedrock fracture spacing arising as a consequence of differing tectonic setting and exhumation history (DiBiase et al., 2018a).

DiBiase et al. (2018a) exploited a measured 5× contrast in fracture density between the NSJM and eastern SGM, and showed how wider fracture spacing in the NSJM results in steeper cliffs, coarser sediment in channels, and consequently steeper channels and lower fluvial drainage density. Here we build on this framework to quantify how a contrast in bedrock fracture density influences soil production efficiency and indirectly controls the efficiency of soil transport through armoring of hillslopes by coarse clasts (Fig. 2).

3. Methods

3.1. Catchment erosion rates from in situ cosmogenic ^{10}Be in stream sediments

We collected 21 new stream sediment samples from steep catchments in the eastern SGM and NSJM to determine erosion rates from detrital in situ cosmogenic ^{10}Be concentrations in quartz (Fig. 3). Out of these 21 new samples, 7 samples in each landscape (14 total) were collected as the sand fraction (250–850 μm) of active channel deposits in small (1–4 km^2) headwater catchments that are mostly nested within larger sampled watersheds (10–20 km^2) (Fig. 2). In one larger watershed from each landscape, we collected 3 separate samples at the same location in the active channel to evaluate the potential for grain-size-dependent exposure histories: one sand-sized fraction sample (250–850 μm), one pebble-sized fraction sample (2–6 cm), and one cobble-sized fraction sample (8–12 cm).

Quartz separation and ^{10}Be extraction were performed at the University of Vermont Community Cosmogenic Facility following standard protocols (Corbett et al., 2016). Quartz was purified by heating the sieved samples in HCl and treating them with a series of leaches using dilute HF/HNO_3 (Kohl and Nishiizumi, 1992). For amalgamated pebble and cobble samples, we

crushed and sieved each sample to 250–850 μm. Quartz yields after etching and mineral separation techniques were 15–30 % of the initial sample mass. We added 240 μg of Be through low-background beryl carrier to each sample, and measured $^{10}Be/^{9}Be$ ratios using accelerator mass spectrometry at the Purdue Rare Isotope Measurement (PRIME) Laboratory, normalizing measured ratios to ICN standard 07KNSTD3110 (2.85×10^{-12}; Nishiizumi et al., 2007). Samples SG1601-02; SG1605-09; and SJ1601-06 were analyzed on July 24, 2017, and ratios were reduced using an average of 6 process blanks ($^{10}Be/^{9}Be = 8.5 \pm 5.4 \times 10^{-16}$, 1SD). All other samples were analyzed on March 25, 2018, with ratios reduced using an average of 5 process blanks ($^{10}Be/^{9}Be = 6.4 \pm 1.3 \times 10^{-16}$, 1SD).

We calculated erosion rates from detrital ^{10}Be concentrations with the CRONUS-Earth online calculator (https://hess.ess.washington.edu/, version 2.3; Balco et al., 2008) using the Lal/Stone constant production rate model (Lal, 1991; Stone, 2000) and standard atmospheric model. We calculated an effective elevation to determine atmospheric attenuation of ^{10}Be production for each sample basin using catchment hypsometry (Portenga and Bierman, 2011). Following DiBiase (2018), we did not apply topographic shielding corrections for calculating catchment-mean erosion rates. We used the same production rate model, atmospheric attenuation scaling, and CRONUS online calculator to recalculate previously published detrital ^{10}Be data (DiBiase et al., 2010, 2012, 2018a; Heimsath et al., 2012; Rossi, 2014) from 17 small headwater catchments (1–4 km^2) and 3 larger catchments (4–28 km^2) in the SGM and NSJM where high-resolution lidar topography is available (Fig. 1; supplementary table S4). Straightforward interpretation of catchment mean erosion rates from detrital in situ ^{10}Be concentrations requires the assumption of a well-mixed sediment sample representative of a catchment with broadly uniform quartz distribution and erosion rate (Bierman and Stieg, 1996). In steep landscapes with

patchy soil cover, we thus assume that bare-bedrock and soil-mantled hillslopes erode at similar rates.

3.2. Surface cover mapping

We defined surface cover on hillslopes as a soil mantle or bare bedrock in ArcGIS (https://www.arcgis.com/) using 6–20 cm resolution georeferenced orthophotos derived from low-altitude commercial aerial imagery (Pictometry Corp. - https://www.eagleview.com/product/pictometry-imagery/) and ground and drone-based imagery surveys where available. The smallest bedrock patches mapped were approximately 25 m^2, and we defined bedrock as in-place rock exposed at the surface, whereas soil cover, scree/talus deposits, and vegetated areas were collectively mapped as soil (Fig. 2; Fig. 4). We mapped regions of low-sloping valley fill and omit these regions from topographic analyses to focus our morphologic analysis on eroding hillslopes only.

Commercial aerial imagery does not cover the most rapidly eroding catchments in the eastern SGM (SG1605 and SG1706). Instead, we generated georeferenced orthophotos from both ground- and drone-based structure-from-motion photogrammetry surveys (James and Robson, 2012). We used a Nikon D5500 digital single-lens reflex camera with a telephoto lens (55 mm focal length) for ground-based imaging, and a DJI Mavic Pro quadcopter for drone-based imaging. Camera alignment and dense point cloud generation were performed in Agisoft PhotoScan v1.4.0 (https://www.agisoft.com/). Initial georeferencing and camera alignment optimization was achieved using GPS information from camera locations (~1 m accuracy for ground-based surveys and ~5 m accuracy for drone-based surveys), and the aligned cameras were used to construct dense point clouds (resolution ~2–5 cm). We then refined the alignment of the dense point clouds through iterative closest point alignment to georeferenced aerial lidar

point clouds (resolution ~10–100 cm) using the software CloudCompare (http://www.cloudcompare.org/). Orthophotos were generated by rasterizing the structure-from-motion-photogrammetry-derived colorized dense point clouds using CloudCompare at a resolution of 15 cm, similar to the quality of orthophotos available from commercial imagery. Occasionally, inspection of original photographs was used to resolve areas with ambiguous surface cover.

Surface cover was mapped across all regions in headwater catchments where high-resolution imagery was available (either from commercial aerial imagery or ground and drone-based surveys). Imagery covered 94% of the headwater catchment area covered by ^{10}Be erosion rate samples in the SGM and 35% of the headwater catchment area covered by ^{10}Be erosion rate samples in the NSJM (Fig. 1; Fig. 3). For headwater catchments with ^{10}Be erosion rates but only partial orthophoto coverage, surface cover was mapped in regions with available orthophoto coverage (>100,000 m^2), and the mean hillslope angle of the region with orthophoto coverage was compared to the mean hillslope angle of the full catchment area upstream from the ^{10}Be sample. In these cases, mean hillslope angles differ by <2° between the region with bedrock exposure mapping and the full catchment sampled by the ^{10}Be erosion rate (Table 1). For these catchments where surface cover mapping was performed over a portion of the watershed (9 out of 29 total catchments), we assumed the surface cover within each representative mapping region reflects that throughout the headwater catchment upstream from the ^{10}Be erosion rate sample.

3.3 Topographic analysis

Local hillslope angle was calculated at each pixel on 1 m resolution airborne-lidar-derived bare-earth digital elevation models (DEMs) by measuring the dip of a plane fit to all neighboring cells within a 15 m diameter spherical window using CloudCompare. Measuring

slope at this scale was found to best reduce noise in lidar DEMs from vegetation while sacrificing the least resolution around the morphology of rough, rocky terrain (Roering, 2008; Supplementary Fig. S1). For all ^{10}Be sample catchments (including catchments without surface cover mapping), we calculated mean hillslope angle and generated hillslope angle distributions using a Gaussian kernel density estimation with a bandwidth of 0.1°.

In the 29 headwater catchments where we mapped surface cover, we separately calculated the mean and distribution of hillslope angles within soil-mantled hillslopes, bare-bedrock hillslopes, and all hillslopes within the catchment (Table 1). For all calculations, we excluded areas of low-sloping valley fill. Additionally, we extended this analysis to small (<1 km^2) rocky areas where surface cover was mapped, but where the area is not directly associated with the extent of a ^{10}Be sample catchment (red outlines, Fig. 3, Supplementary Table S2).

To compare the morphology of steep, headwater catchments in the SGM and NSJM, we compared the hillslope angle distributions of full catchments, soil-mantled hillslopes, and bare-bedrock hillslopes from the SGM and NSJM. We focused on the same range of steep headwater catchments in the SGM and NSM where bedrock exposure is abundant (mean slope >35°). We weighted the catchment erosion rate and slope distributions of soil-mantled, bare-bedrock, and full catchments by the aerial extent of the region where soil and bedrock was mapped in each headwater catchment (Fig. 3). These distributions show the overall difference between the SGM and NSJM in percent bedrock exposure on hillslopes, soil-mantled hillslope morphology, and bedrock hillslope morphology.

3.4 Non-linear soil transport model

We used the 1D hillslope-averaged form of a non-linear soil transport model (Roering et al., 1999; 2007) to quantify contrasts in soil-mantled hillslope morphology and erosion rate between the SGM and NSJM, defined by:

$$S_{ave} = S_c \frac{1}{E^*}\left(\sqrt{1 + (E^*)^2} - \ln\left(\frac{1}{2}\left(1 + \sqrt{1 + (E^*)^2}\right)\right) - 1\right), \quad (1a)$$

$$E^* = \frac{2E\left(\rho_r/\rho_s\right)L_H}{KS_c}, \quad (1b)$$

where S_{ave} is the mean hillslope gradient (m/m) of the soil mantled hillslopes, S_c is a critical gradient (m/m) related to soil stability, E is the bedrock erosion rate, ρ_r/ρ_s is the ratio of rock to soil density, L_H is hillslope length, and K is the soil transport efficiency, which describes how soil flux, q_s, varies with local slope, S, following Roering et al. (1999):

$$q_s = \frac{-KS}{1-(S/S_c)^2}. \quad (2)$$

Whereas Equation (1) is typically applied to the relationship between catchment-mean hillslope angle and ^{10}Be-derived erosion rate (e.g., DiBiase et al., 2010), we used the results from our surface cover mapping to isolate the relationship between erosion rate and the morphology of the soil-mantled parts of each catchment. We made two key assumptions. First, we assumed that the mean gradient of soil-mantled areas is equivalent to S_{ave}, the mean hillslope gradient of a steady-state, 1D hillslope profile (i.e., bedrock exposure is not systematically correlated with hillslope position; Supplementary Fig. S2). Second, we assumed that erosion rates are spatially uniform within each catchment (i.e., similar for soil-mantled and rocky parts of the catchment), based on the similarity of soil-production rates on slopes with thin soils and no soil cover in the SGM, which match catchment erosion rates (Heimsath et al., 2012). Additionally, we find no systematic variation in ^{10}Be concentration among multiple-grain size samples in either the SGM or NSJM (Table S1). We assumed that hillslope length (L_H = 100 m – DiBiase et al., 2012), the

ratio of rock to soil density (ρ_r/ρ_s = 2), and the critical slope for soil (S_c = 45°) are similar between the SGM and NSJM, and we determined the best fit value of the soil transport efficiency, K, for both landscapes, minimizing the root mean square error, $RMSE$, between the measured and modeled erosion rates:

$$RMSE = \sqrt{\frac{1}{N}\sum_{n=1}^{N}\frac{(\log E_{measured}(n) - \log E_{modeled}(n))^2}{\log \sigma(n)}}, \quad (3)$$

where $E_{measured}$ and $E_{modeled}$ are the measured erosion rates and erosion rates predicted by Equation (1), respectively, σ is the 1-sigma analytical error of the measured erosion rate, and N is the number of samples. The log-transformation approximates the non-linear form of the soil transport model and normalizes erosion rate residuals such that background residuals do not vary systematically with mean slope.

4. Results

4.1 Surface cover mapping

Of the steep (S_{ave} > 35°) headwater catchments mapped in detail, 48% of NSJM hillslopes and 21% of SGM hillslopes are bare bedrock (Fig. 5). In these mapped regions, the mean hillslope angle of soil mantled areas is 2° steeper in the NSJM (39°) than the SGM (37°). Overall, mean bare-bedrock slopes are 8–9° steeper than soil mantled hillslopes, and the mean slope of bare-bedrock areas are 3° steeper in the NSJM (48°) than the SGM (45°) (Fig. 5).

For both landscapes, bedrock exposure is limited to occasional tors in catchments with mean hillslope angles less than 35° (Fig. 2, Fig. 6a); for hillslopes with mean hillslope angles greater than 35° there is a strong positive relationship between the fraction of exposed bedrock and mean hillslope angle (r^2 = 0.81, $p < 0.01$ in SGM; r^2 = 0.73, $p < 0.01$ in NSJM) (Fig. 6a). Extrapolating the relationship between mean hillslope angle and fraction of exposed bedrock in

each landscape, mean hillslope angles of 49° and 57° are predicted for 100% bare-bedrock hillslopes in the SGM and NSJM, respectively. Between both landscapes, there is no systematic trend between fraction of exposed bedrock and mean annual precipitation or elevation (Fig. 6b; Fig. 6c). In the NSJM, the fraction of exposed bedrock decreases in wetter catchments ($r^2 = 0.27$, $p = 0.06$), but in the SGM, the fraction of exposed bedrock increases in wetter catchments ($r^2 = 0.54$, $p < 0.01$).

4.2 Catchment erosion rates, hillslope morphology, and bedrock exposure

Catchment-mean erosion rates generally increase with increasing mean hillslope angle in both landscapes, and for a given mean hillslope angle, erosion rates are 2-5× higher in the SGM than the NSJM (Fig. 7a). This contrast is most pronounced in steep, rocky catchments (mean hillslope angle >35°). In the NSJM, erosion rates in steep, rocky catchments range from 0.1–0.6 m kyr^{-1}, and catchment mean hillslope angles range from 39–46°; steep, rocky catchments in the SGM exhibit erosion rates ranging from 0.2–2.2 m kyr^{-1} and catchment mean hillslope angles ranging from 36–45°. A strong positive correlation ($r^2 = 0.88$, $p < 0.01$) between mean hillslope angle and erosion rate derived from catchments elsewhere in the SGM (DiBiase et al., 2010; 2012) extends into the steeper landscapes of the eastern SGM, and for steep (S_{ave} >35°) headwater catchment samples in the SGM, there exists a positive correlation between mean hillslope angle and erosion rate ($r^2 = 0.56$, $p = 0.02$). The correlation between mean hillslope angle and erosion rate is weaker for steep catchments in the NSJM ($r^2 = 0.33$, $p = 0.1$), but nested samples collected within the same catchment record consistent erosion rates (Fig. 3, Table S1). ^{10}Be concentrations measured from sand, pebble, and cobble samples do not show systematic variations with grain size fraction, and differ by a maximum of 38% in the NSJM and a maximum of 35% in the SGM (Table S1).

Three lines of evidence suggest that our interpretation of erosion rates in the SGM and NSJM are robust. First, inspection of nested samples from the eastern SGM and NSJM (Fig. 3; Table S1) indicates that the ^{10}Be concentration of downstream samples are consistent with upstream nested samples, indicating that sediment in the larger catchments is well-mixed. Second, the positive correlation between erosion rate and mean hillslope angle for headwater catchments in the SGM ($r^2 = 0.56$, $p = 0.02$) (Fig. 7a) suggests that erosion rates primarily record spatial changes in hillslope morphology and not stochastic input of ^{10}Be-diluted material from deep landslides (e.g., Yanites et al., 2009). Landslide mapping in the eastern San Gabriel Mountains indicates that landslides deeper than 3-5 m are both uncommon over the integration area (1-10 km^2) and timescale (~300-3000 yr for erosion of one e-folding depth) of our detrital ^{10}Be samples (Lavé and Burbank, 2004) and tend to leave distinct morphologic signatures not seen in these catchments (Scherler et al., 2016). The correlation between erosion rate and mean hillslope angle is less significant for headwater catchments in the NSJM (Fig. 7a), a point which we expand upon in Section 5.2 below. Third, the absence of a clear dependence on grain size from multiple grain size samples in the eastern SGM and NSJM suggests a similar residence time of sand, pebbles, and cobbles on hillslopes. Assuming that coarser clasts are preferentially sourced from rocky hillslopes in both landscapes (Sklar et al., 2017), the similarity of in-situ ^{10}Be concentrations measured from detrital sand, pebble, and cobble samples is consistent with bedrock hillslopes and soil mantled hillslopes eroding at similar rates.

In both landscapes, the non-linear soil transport model broadly captures the relationship between erosion rate and the mean hillslope angle of soil-mantled regions; however, for the same mean hillslope angle, soil-mantled hillslopes in the SGM are eroding 2–3× faster than those in the NSJM, as reflected by a 2–3× difference in the best-fit soil transport efficiency, K (Fig. 7b).

In both landscapes the mean hillslope angles of bare bedrock regions typically exceed the assumed critical slope for soils, S_c, and bare bedrock hillslopes are steeper in the NSJM than the SGM.

Extensive bedrock exposure on hillslopes (>20%) occurs in both landscapes when mean hillslope angles exceed ~35° (Fig. 6a), and this hillslope morphology coincides with catchment erosion rates of ~0.1 m kyr^{-1} and ~0.2 m kyr^{-1} in the NSJM and SGM, respectively (Fig. 8). At the scale of headwater catchments (1–4 km^2), most regions in the NSJM and SGM are characterized by a patchwork of bedrock cliffs and soil-mantled hillslopes, and even for the steepest, most rapidly eroding regions of both landscapes (NSJM = 0.6 m kyr^{-1}, SGM = 2.2 m kyr^{-1}), a soil mantle is retained on ~30–50% of hillslopes. Generally, bedrock exposure continues to increase with higher erosion rates in both landscapes, but for catchments with similar erosion rate, bedrock exposure on hillslopes is greater in NSJM catchments than SGM catchments (Fig. 8).

5. Discussion

5.1 Controls on the relationship between hillslope morphology, bedrock exposure, and erosion rate

We interpret that the contrast in erosion rate, bedrock exposure, and hillslope morphology is primarily due to an observed 5× contrast in bedrock fracture density between the NSJM and SGM (DiBiase et al., 2018a), rather than differences in mean annual precipitation. Although differences in climate between the SGM and NSJM could influence relationships between hillslope morphology, bedrock exposure, and erosion rate, there is a weak and inconsistent effect of mean annual precipitation expressed in our data. Bedrock exposure and mean annual precipitation are directly correlated in the SGM because wetter catchments in the SGM typically

have steeper hillslope angles, but bedrock exposure and mean annual precipitation are inversely correlated in the NSJM because wetter catchments in the NSJM typically have gentler hillslope angles (Fig. 6). The opposing dependence between mean annual precipitation and bedrock exposure between these two landscapes suggests that climate drivers of bedrock exposure are secondary to rock strength, topographic, and erosional drivers of bedrock exposure (Fig. 6a, Fig. 8). A direct rock strength control on rock exposure is also supported by observations that ~3× more bedrock hillslopes are exposed in the NSJM than the SGM when comparing between catchments in the NSJM and SGM that have similar topography and mean annual precipitation (Supplementary Fig. S3). Below, we use our data from the SGM and NSJM to show how bedrock fracture density influences soil production rate (Section 5.1.1), the efficiency of soil transport (Section 5.1.2), and the limits to bedrock cliff stability (Section 5.1.3), and how these effects interact to determine the relationship between hillslope morphology and erosion rate.

5.1.1. Soil production efficiency contrast between NSJM and SGM

Our catchment-scale erosion rates paired with observations of similarly thin and patchy soil cover in both the SGM and NSJM indicate that a first-order contrast in soil production efficiency is driven by a difference in bedrock fracture spacing. In both landscapes, systematic bedrock exposure occurs at similar hillslope morphology (Fig. 6A), but at a higher erosion rate in the SGM than the NSJM (Fig. 8), indicating higher soil production rates in the SGM for similarly thin and patchy soils (Fig. 2). For similar catchment erosion rates, hillslopes in the SGM have less bedrock exposed than hillslopes in the NSJM, indicating consistently higher soil production efficiency in the SGM (Fig. 8). We attribute the increased soil production efficiency in the SGM to the 5× denser fracture spacing observed in exposed bedrock cliffs of the SGM relative to the NSJM (Fig. 2; DiBiase et al., 2018a). Sparse bedrock fracture spacing in the NSJM likely limits

the extent of water-rock interactions in the near surface that drive chemical weathering and soil production (e.g., Fletcher and Brantley, 2010). Additionally, mechanical processes that mobilize fractured bedrock (e.g., detachment by tree roots) are expected to decrease in efficiency with decreased bedrock fracture density (Graham et al., 2010).

5.1.2. Soil transport efficiency contrast between NSJM and SGM

Soil-mantled hillslopes in the SGM near the soil threshold stability angle, S_c, yield erosion rates that are ~3× higher than erosion rates measured on similarly steep hillslopes in the NSJM (Fig. 7b), indicating increased soil transport efficiency (3× higher K, Equation 2) in the SGM. Alternatively, the higher erosion rates for a given mean soil-mantled hillslope angle in the SGM could arise from shorter hillslopes (i.e., 3× lower L_H, Equation 1b). Quantifying L_H in the SGM and NSJM is problematic due to challenges in delineating hillslopes and channels in rocky landscapes (DiBiase et al., 2012); yet, qualitative inspection of slope and hillshade maps from both landscapes reveals that valley spacing (and thus hillslope length) does not systematically vary between the SGM and NSJM, and thus we interpret our data as primarily reflecting a contrast in soil transport efficiency, K. Although we interpret our data using the 1D steady-state form of a nonlinear soil transport model (Roering et al., 1999; 2007), we acknowledge that there is a limitation to applying this model on patchy hillslopes. Regardless of the hillslope transport model used, an effective 3× contrast in soil transport efficiency is required to reconcile low erosion rates measured in the NSJM.

Whereas the control on soil production rates can be directly sensitive to bedrock fracture density, the morphology of soil mantled hillslopes tends to less directly reflect rock material properties. However, we observe a contrast in the surface texture of soils that mirrors the contrast in fracture density between the two landscapes. Compared to hillslopes in the SGM, hillslopes in

423 the NSJM are characterized by more abundant bedrock cliffs with wider fracture spacing that
424 deliver larger clasts to steep soil-mantled hillslopes (Fig. 2), and we interpret this grain size
425 difference to drive a contrast in soil transport efficiency between the SGM and NSJM (e.g.,
426 Glade et al., 2017; DiBiase et al, 2018b). Coarser sediment armor decreases bioturbation
427 efficiency, increases hillslope roughness (DiBiase et al., 2017), and decreases sediment transport
428 by overland flow (Michaelides and Martin, 2012). Additionally, increased frequency and
429 intensity of wildfires and/or co-seismic shaking (Sleep, 2011) in the SGM could increase
430 hillslope disturbance and transport rates (and thus increase the soil transport coefficient, K)
431 relative to the NSJM.

432 *5.1.3. Soil and rock stability angles in the SGM and NSJM*

433 The critical slope for soil stability, S_c, appears similar between the NSJM and SGM,
434 based on the similarity in catchment hillslope morphology associated with the onset of
435 significant hillslope bedrock exposure (Fig. 6a). Thus, although the observed contrast in surface
436 material grain size strongly influences the relationship between soil-mantled hillslope
437 morphology and erosion rate (Fig. 7b), the maximum soil-mantled hillslope angle does not
438 appear to be sensitive to grain size, in agreement with prior interpretations of a friction-
439 dominated transition from soil-mantled to bedrock hillslopes above an angle of repose in the
440 SGM (DiBiase et al., 2012; DiBiase et al., 2017).

441 Whereas the SGM and NSJM exhibit a similar threshold for soil-mantled hillslope
442 steepness, widely-spaced bedrock fractures in the NSJM support steeper and taller bedrock cliffs
443 than those in the SGM (Fig. 2; DiBiase et al., 2018a). Extrapolation of the relationship between
444 percent bedrock exposure and catchment mean slope to 100% bedrock yields a higher mean
445 bedrock hillslope angle in the NSJM (57°) than in the SGM (49°) (Fig. 6a). The observation of

overall steeper bedrock hillslopes in the NSJM is consistent with analysis of individual cliffs in the eastern SGM and NSJM, which showed that the steepest bedrock cliffs in the NSJM exhibit an effective cohesion 3× higher than the steepest cliffs in the eastern SGM (DiBiase et al., 2018a). Because steep hillslopes are near threshold conditions, the mean slope of bedrock and soil-mantled hillslopes changes little for progressive increases in erosion rate in both landscapes. However, wider fracture spacing decreases soil production efficiency and strengthens cliffs in the NSJM relative to the SGM, so more abundant and steeper cliffs are exposed in the NSJM than the SGM for a given increase in catchment erosion rate, yielding a more rapid increase in catchment-mean slope in the NSJM than the SGM for a progressive increase in erosion rate (Fig. 7a).

5.2 Implications of patchy hillslopes for rock strength controls on landscape evolution

Climatic, ecologic, and lithologic controls on the relative abundance of bare bedrock and soil cover are important considerations when applying hillslope evolution models that assume a continuous soil mantle and a single hillslope erodibility. For example, we isolate a contrast in bedrock fracture spacing between the NSJM and SGM and show that the transition from soil-mantled to bare-bedrock landscapes occurs at different erosion rates in these two landscapes (Fig. 8). A hillslope transport model derived for soil-mantled hillslopes can describe soil-mantled landscapes in the SGM until significant bedrock is exposed when erosion rates exceed ~0.2 m kyr^{-1}, but soil-mantled landscapes transition to patchy soil-mantled and bare-bedrock landscapes at erosion rates as low as ~0.1 m kyr^{-1} in the NSJM (Fig. 7).

Globally, soil production rates vary by over three orders of magnitude (Heimsath et al., 2012; Larsen et al., 2014), and the transition from soil-mantled to bare-bedrock landscapes occurs across a similarly wide range of catchment erosion rates (Fig. 8). We argue that the

contrast in soil production efficiency between the SGM and NSJM arises due to differences in bedrock fracture density. However, analysis of patchy soil and bedrock hillslopes in the Sierra Nevada, CA and Southern Alps, NZ suggest that soil production efficiency may be equally sensitive to bedrock mineralogy (Hahm et al., 2014) and/or climate (Larsen et al., 2014) (Fig. 8). These dependencies between climate, ecology, lithology and the relative abundance of bare bedrock and soil cover contribute to scatter in hillslope erodibility seen in global compilations (Portenga and Bierman, 2011) and show additional controls on catchment-averaged soil thickness, which has implications for the strength of silicate weathering feedbacks in the context of global climate models (West, 2012).

Because soil and bedrock can have strongly contrasting strength, a hillslope transport model incorporating a single threshold morphology for either soil (e.g., Roering et al., 1999) or bedrock (e.g., Schmidt and Montgomery, 1995) is insufficient to characterize the evolution of steep landscapes that commonly consist of a patchwork of rock and soil. The inferred critical slope for bedrock hillslopes is 57° in the NSJM and 49° in the SGM, which is steeper than the critical slope of soil mantled hillslopes in both landscapes (S_c = 45°). Thus, there is a range of bedrock hillslope morphology that exceeds the strength limitations of soils but is below the strength limitations of bedrock (e.g., Schmidt and Montgomery, 1995).

For landscapes with relatively weak bedrock (e.g., SGM), there is a narrow window of bedrock hillslope morphology, because the threshold slope for weak bedrock only slightly exceeds the threshold slope for soil stability. For landscapes with relatively strong bedrock (e.g., NSJM), there is a wider range of bedrock cliff morphology that we hypothesize contributes to scatter in the relationship between catchment mean slope and erosion rate (Fig. 7a). Over longer timescales, it is unclear how the slope of these cliff faces could be reduced to a slope gentle

enough to support a stable soil mantle. Cliffs in landscapes with strong bedrock may persist long after they were originally exposed, and the contrast in threshold stability angles between soil and bedrock hillslopes may explain why high cliff abundance and high relief persist in some post-orogenic systems, even though active tectonics have long-ceased and erosion rates are relatively low (e.g., Scharf et al., 2013).

Conclusions

Our analysis shows how the morphology of steep landscapes comprising a patchwork of soil-mantled and bare-bedrock hillslopes varies with erosion rate and bedrock fracture density. In both the San Gabriel Mountains and Northern San Jacinto Mountains of California, hillslopes are progressively steeper and rockier in headwater catchments with higher erosion rates. However, despite lower erosion rates, hillslopes in the San Jacinto Mountains are steeper and rockier than those in the San Gabriel Mountains, indicating more efficient soil production from the highly fractured bedrock of the San Gabriel Mountains. Additionally, for similar soil-mantled hillslope morphology, erosion rates are 3× higher in the San Gabriel Mountains than in the Northern San Jacinto Mountains. We interpret the resulting 3× contrast in soil transport efficiency to reflect a difference in the size of coarse material armoring hillslopes, which depends in part on bedrock fracture density. Together, these data highlight the limitations of hillslope transport models that incorporate a single threshold morphology for soil or bare rock. Rather, understanding the morphodynamics of steep landscapes and their sensitivity to rock properties requires the partitioning of the controls on soil production, soil transport, and the relative strength of soil and rock.

Acknowledgments

514 This project was supported by National Science Foundation grant EAR-1608014 to R. DiBiase.
515 Cosmogenic data was generated with the support of NSF-EAR 1735676 to P. Bierman. AMS
516 measurements were supported in part by NSF EAR-1560658 to M. Caffee. Airborne lidar was
517 flown and processed by the National Center for Airborne Laser Mapping, with support from
518 Pennsylvania State University. Low-altitude aerial imagery was acquired by Pictometry
519 Corporation. We thank J. Carr, J. Del Vecchio, E. Greenberg, and P. Silverhart for field
520 assistance. J. Carr operated the drone and collected photographs for building structure-from-
521 motion models. We thank M. Campbell for assisting with sample preparation. We commend
522 McLanahan's downtown market for providing a comfortable workspace during the preparation
523 of this manuscript. Comments from I. Larsen and one anonymous reviewer helped improve the
524 manuscript.

References

Balco, G., Stone, J.O., Lifton, N.A. and Dunai, T.J., 2008. A complete and easily accessible means of calculating surface exposure ages or erosion rates from ^{10}Be and ^{26}Al measurements. Quaternary geochronology, 3(3), pp.174-195. https://doi.org/10.1016/j.quageo.2007.12.001

Bierman, P. and Steig, E.J., 1996. Estimating rates of denudation using cosmogenic isotope abundances in sediment. Earth surface processes and landforms, 21(2), pp.125-139. https://doi.org/10.1002/(SICI)1096-9837(199602)21:2<125::AID-ESP511>3.0.CO;2-8

Blythe, A.E., House, M.A. and Spotila, J.A., 2002. Low-temperature thermochronology of the San Gabriel and San Bernardino Mountains, southern California: Constraining structural evolution. Special Papers-Geological Society of America, pp.231-250. http://resolver.caltech.edu/CaltechAUTHORS:20150209-154220360

Carson, M. A. & Kirby, M. J. Hillslope Form and Process (Cambridge Univ. Press, Cambridge, 1972).

Coe, J.A., Kinner, D.A. and Godt, J.W., 2008. Initiation conditions for debris flows generated by runoff at Chalk Cliffs, central Colorado. Geomorphology, 96(3-4), pp.270-297. https://doi.org/10.1016/j.geomorph.2007.03.017

Corbett, L.B., Bierman, P.R. and Rood, D.H., 2016. An approach for optimizing in situ cosmogenic ^{10}Be sample preparation. Quaternary Geochronology, 33, pp.24-34. https://doi.org/10.1016/j.quageo.2016.02.001

Critchfield, W.B., 1971. Profiles of California vegetation. Res. Paper PSW-RP-76. Berkeley, CA: Pacific Southwest Forest & Range Experiment Station, Forest Service, US

Department of Agriculture; 54 p, 76. https://www.fs.fed.us/psw/publications/documents/psw_rp076/psw_rp076.pdf

Crook, R., Jr., Allen, C.R., Kamb, B., Payne, C.M. and Serra Proctor, R.J., 1987. Quaternary geology and seismic hazard of the Sierra Madre and associated faults, western San Gabriel Mountains, in Recent Reverse Faulting in the Transverse Ranges, California, edited by D.M. Morton and R.F. Yerkes, U.S. Geol. Surv. Prof. Pap., 1339, 179-203. http://resolver.caltech.edu/CaltechAUTHORS:20150709-101959806

DiBiase, R.A., 2018. Increasing vertical attenuation length of cosmogenic nuclide production on steep slopes negates topographic shielding corrections for catchment erosion rates. Earth Surface Dynamics, 6(4), pp. 923-931. https://doi.org/10.5194/esurf-6-923-2018

DiBiase, R.A., Whipple, K.X., Heimsath, A.M. and Ouimet, W.B., 2010. Landscape form and millennial erosion rates in the San Gabriel Mountains, CA. Earth and Planetary Science Letters, 289(1-2), pp.134-144. https://doi.org/10.1016/j.epsl.2009.10.036

DiBiase, R.A., Heimsath, A.M. and Whipple, K.X., 2012. Hillslope response to tectonic forcing in threshold landscapes. Earth Surface Processes and Landforms, 37(8), pp.855-865. https://doi.org/10.1002/esp.3205

DiBiase, R.A., Lamb, M.P., Ganti, V. and Booth, A.M., 2017. Slope, grain size, and roughness controls on dry sediment transport and storage on steep hillslopes. Journal of Geophysical Research: Earth Surface, 122(4), pp.941-960. https://doi.org/10.1002/2016JF003970

DiBiase, R.A., Rossi, M.W. and Neely, A.B., 2018. Fracture density and grain size controls on the relief structure of bedrock landscapes. Geology, 46(5), pp.399-402. https://doi.org/10.1130/G40006.1

569 DiBiase, R.A., Denn, A.R., Bierman, P.R., Kirby, E., West, N. and Hidy, A.J., 2018.
570 Stratigraphic control of landscape response to base-level fall, Young Womans Creek,
571 Pennsylvania, USA. Earth and Planetary Science Letters, 504, pp.163-173.
572 https://doi.org/10.1016/j.epsl.2018.10.005
573 Dietrich, W.E., Bellugi, D.G., Sklar, L.S., Stock, J.D., Heimsath, A.M. and Roering, J.J., 2003.
574 Geomorphic transport laws for predicting landscape form and dynamics. Prediction in
575 geomorphology, 135, pp.103-132. https://doi.org/10.1029/135GM09
576 Dixon, J.L. and von Blanckenburg, F., 2012. Soils as pacemakers and limiters of global silicate
577 weathering. Comptes Rendus Geoscience, 344(11-12), pp.597-609.
578 https://doi.org/10.1016/j.crte.2012.10.012
579 Dixon, J.L., Hartshorn, A.S., Heimsath, A.M., DiBiase, R.A. and Whipple, K.X., 2012. Chemical
580 weathering response to tectonic forcing: A soils perspective from the San Gabriel
581 Mountains, California. Earth and Planetary Science Letters, 323, pp.40-49.
582 and Soil, 403, 7–20. https://doi.org/10.1016/j.epsl.2012.01.010
583 Fletcher, R.C. and Brantley, S.L., 2010. Reduction of bedrock blocks as corestones in the
584 weathering profile: observations and model. American Journal of Science, 310(3),
585 pp.131-164. https://doi.org/10.2475/03.2010.01
586 Glade, R.C., Anderson, R.S. and Tucker, G.E., 2017. Block-controlled hillslope form and
587 persistence of topography in rocky landscapes. Geology, 45(4), pp.311-314.
588 https://doi.org/10.1130/G38665.1
589 Graham, C.R., Rossi, M.A., Hubbert, R.K., 2010. Rock to regolith conversion: Producing
590 hospitable substrates for terrestrial ecosystems. GSA today, 20(2), p.5.
591 https://doi.org/10.1130/GSAT57A.1

592 Granger, D.E., Riebe, C.S., Kirchner, J.W. and Finkel, R.C., 2001. Modulation of erosion on
593 steep granitic slopes by boulder armoring, as revealed by cosmogenic 26Al and 10Be.
594 Earth and Planetary Science Letters, 186(2), pp.269-281. https://doi.org/10.1016/S0012-
595 821X(01)00236-9
596 Hahm, W.J., Riebe, C.S., Lukens, C.E. and Araki, S., 2014. Bedrock composition regulates
597 mountain ecosystems and landscape evolution. Proceedings of the National Academy of
598 Sciences, 111(9), pp.3338-3343. https://doi.org/10.1073/pnas.1315667111
599 Heimsath, A.M., Dietrich, W.E., Nishiizumi, K. and Finkel, R.C., 1997. The soil production
600 function and landscape equilibrium. Nature, 388(6640), p.358.
601 https://doi.org/10.1038/41056
602 Heimsath, A.M., DiBiase, R.A. and Whipple, K.X., 2012. Soil production limits and the
603 transition to bedrock-dominated landscapes. Nature Geoscience, 5(3), p.210. DOI:
604 10.1038/NGEO1380
605 James, M.R. and Robson, S., 2012. Straightforward reconstruction of 3D surfaces and
606 topography with a camera: Accuracy and geoscience application. Journal of Geophysical
607 Research: Earth Surface, 117(F3). https://doi.org/10.1029/2011JF002289
608 Jennings, C.W., Strand, R.G., and Rogers, T.H., 1977, Geologic map of California: California
609 Division of Mines and Geology, scale 1:750,000.
610 Kohl, C.P. and Nishiizumi, K., 1992. Chemical isolation of quartz for measurement of in-situ-
611 produced cosmogenic nuclides. Geochimica et Cosmochimica Acta, 56(9), pp.3583-
612 3587. https://doi.org/10.1016/0016-7037(92)90401-4

613 Korup, O., 2008. Rock type leaves topographic signature in landslide-dominated mountain
614 ranges, Geophysical Research Letters, 35, L11402.
615 https://doi.org/10.1029/2008GL034157
616 Lal, D., 1991. Cosmic ray labeling of erosion surfaces: in situ nuclide production rates and
617 erosion models. Earth and Planetary Science Letters, 104(2-4), pp.424-439.
618 https://doi.org/10.1016/0012-821X(91)90220-C
619 Larsen, I.J., Almond, P.C., Eger, A., Stone, J.O., Montgomery, D.R. and Malcolm, B., 2014.
620 Rapid soil production and weathering in the Western Alps, New Zealand. Science,
621 p.1244908. DOI: 10.1126/science.1244908
622 Lavé, J. and Burbank, D., 2004. Denudation processes and rates in the Transverse Ranges,
623 southern California: Erosional response of a transitional landscape to external and
624 anthropogenic forcing. Journal of Geophysical Research: Earth Surface, 109(F1).
625 https://doi.org/10.1029/2003JF000023
626 Michaelides , K., and Martin, G. J., 2012. Sediment transport by runoff on debris-mantled
627 dryland hillslopes. Journal of Geophysical Research: Earth Surface, 117, F03014.
628 https://doi.org/10.1029/2012JF002415
629 Milodowski, D.T., Mudd, S.M. and Mitchard, E.T.A., 2015. Topographic roughness as a
630 signature of the emergence of bedrock in eroding landscapes. Earth Surface Dynamics,
631 3(4), pp.483-499. https://doi.org/10.5194/esurf-3-483-2015
632 Moore, J.R., Sanders, J.W., Dietrich, W.E. and Glaser, S.D., 2009. Influence of rock mass
633 strength on the erosion rate of alpine cliffs. Earth Surface Processes and Landforms,
634 34(10), pp.1339-1352. https://doi.org/10.1002/esp.1821

Nishiizumi, K., Imamura, M., Caffee, M.W., Southon, J.R., Finkel, R.C. and McAninch, J., 2007. Absolute calibration of 10Be AMS standards. Nuclear Instruments and Methods in Physics Research Section B: Beam Interactions with Materials and Atoms, 258(2), pp.403-413. https://doi.org/10.1016/j.nimb.2007.01.297

Portenga, E.W. and Bierman, P.R., 2011. Understanding Earth's eroding surface with ^{10}Be. GSA today, 21(8), pp.4-10. http://dx.doi.org/10.1130/G111A.1

Roering, J.J., Kirchner, J.W. and Dietrich, W.E., 1999. Evidence for nonlinear, diffusive sediment transport on hillslopes and implications for landscape morphology. Water Resources Research, 35(3), pp.853-870. https://doi.org/10.1029/1998WR900090

Roering, J.J., Perron, J.T. and Kirchner, J.W., 2007. Functional relationships between denudation and hillslope form and relief. Earth and Planetary Science Letters, 264(1-2), pp.245-258. https://doi.org/10.1016/j.epsl.2007.09.035

Roering, J.J., 2008. How well can hillslope evolution models "explain" topography? Simulating soil transport and production with high-resolution topographic data. Geological Society of America Bulletin, 120(9-10), pp.1248-1262. https://doi.org/10.1130/B26283.1

Rossi, M.W., 2014, Hydroclimatic Controls on Erosional Efficiency in Mountain Landscapes [Ph.D. Thesis]: Tempe, Arizona, Arizona State University.

Scharf, T.E., Codilean, A.T., De Wit, M., Jansen, J.D. and Kubik, P.W., 2013. Strong rocks sustain ancient postorogenic topography in southern Africa. Geology, 41(3), pp.331-334. https://doi.org/10.1130/G33806.1

Scherler, D., Lamb, M.P., Rhodes, E.J. and Avouac, J.P., 2016. Climate-change versus landslide origin of fill terraces in a rapidly eroding bedrock landscape: San Gabriel River, California. GSA Bulletin, 128(7-8), pp.1228-1248. https://doi.org/10.1130/B31356.1

Schmidt, K.M. and Montgomery, D.R., 1995. Limits to relief. Science, 270(5236), pp.617-620. DOI: 10.1126/science.270.5236.617

Selby, M.J., 1982. Controls on the stability and inclinations of hillslopes formed on hard rock. Earth Surface Processes and Landforms, 7(5), pp.449-467. https://doi.org/10.1002/esp.3290070506

Sklar, L.S., Riebe, C.S., Marshall, J.A., Genetti, J., Leclere, S., Lukens, C.L. and Merces, V., 2017. The problem of predicting the size distribution of sediment supplied by hillslopes to rivers. Geomorphology, 277, pp.31-49. https://doi.org/10.1016/j.geomorph.2016.05.005

Sleep, N.H., 2011. Deep-seated downslope slip during strong seismic shaking. Geochemistry, Geophysics, Geosystems, 12(12). https://doi.org/10.1029/2011GC003838

Stone, J.O., 2000. Air pressure and cosmogenic isotope production. Journal of Geophysical Research: Solid Earth, 105(B10), pp.23753-23759. https://doi.org/10.1029/2000JB900181

West, A.J., 2012. Thickness of the chemical weathering zone and implications for erosional and climatic drivers of weathering and for carbon-cycle feedbacks. Geology 40(9), pp.811-814. https://doi.org/10.1130/G33041.1

Yanites, B.J., Tucker, G.E. and Anderson, R.S., 2009. Numerical and analytical models of cosmogenic radionuclide dynamics in landslide-dominated drainage basins. Journal of Geophysical Research: Earth Surface, 114(F1). https://doi.org/10.1029/2008JF001088

Yule, D. and Sieh, K., 2003. Complexities of the San Andreas fault near San Gorgonio Pass: Implications for large earthquakes. Journal of Geophysical Research: Solid Earth, 108(B11). https://doi.org/10.1029/2001JB000451

Table 1. Catchment-scale bedrock exposure, hillslope morphology, and precipitation.

Larger watersheds[1]	Drainage Area (km^2)	MAP (mm)[3]	Mean hillslope angle (Full catchment)[4]	Erosion rate (m kyr^{-1})					
SG1602	12.4	1163	38.9	1.28 ± 0.19					
SG1608	4.3	1302	38.8	0.63 ± 0.09					
SJC0806[a]	28.2	491	33.8	0.151 ± 0.012					
SJ1606	9.0	529	39.8	0.27 ± 0.03					
SJC0807[a]	11.1	437	35.6	0.086 ± 0.008					
SJ1703	9.8	390	44.4	0.53 ± 0.07					
SJC0802[a]	9.8	390	44.4	0.196 ± 0.021					
SJC0801[a]	6.5	808	18.4	0.040 ± 0.003					
Headwater catchments[2]	**Drainage area (km^2)**	**MAP (mm)**	**Mean hillslope angle (Full catchment)**	**Erosion rate (m kyr^{-1})**	**Mean elevation (m)**	**% Catchment with surface cover mapping**	**% Bedrock exposure**	**Mean Hillslope Angle (Soil-Mantled)[5]**	**Mean Hillslope Angle (Bedrock)[6]**
SG1705	1.9	1292	38.4	0.39 ± 0.05	2275	100	41	36.2	43.0
SG1609	0.80	1319	40.6	0.60 ± 0.07	2312	100	43	37.5	46.3
SG1703	1.3	1042	37.5	0.234 ± 0.024	2088	100	23	35.5	44.2
SG1601	1.2	887	42.2	0.96 ± 0.16	1595	100	23	40.8	47.4
SG1605	1.2	1196	42.3	2.2 ± 0.4	2044	22	60	37.5	44.5
SG1706	1.2	1308	45.0	1.39 ± 0.19	2249	13	68	40.4	47.2
SG125[b]	1.9	905	36.6	0.43 ± 0.05	1333	100	5	36.1	45.1
SG126[b]	2.2	893	38.5	0.54 ± 0.06	1357	100	8	37.8	46.4
SG127[b]	2.5	911	39.9	0.68 ± 0.08	1345	100	25	37.6	47.4
SG128[b]	2.1	716	15.2	0.036 ± 0.004	1789	100	4	15.0	-
SG129[b]	0.13	729	17.2	0.042 ± 0.013	1790	100	19	16.6	20.1
SG131[b]	2.2	677	18.9	0.085 ± 0.013	1737	100	1	18.8	-
SG132[b]	1.1	659	20.8	0.093 ± 0.009	1732	100	1	20.8	-
SG136[b]	0.11	635	25.4	0.120 ± 0.011	2274	100	0	25.4	-
SG151[b]	3.4	988	31.3	0.36 ± 0.12	2291	100	4	30.9	-
SG205[b]	0.11	652	16.5	0.096 ± 0.010	1692	100	0	16.5	-
SGB-7[b]	3.1	794	36.6	0.22 ± 0.04	1315	100	12	36.0	40.8
SG07-01[b]	0.17	633	16.5	0.104 ± 0.009	1677	100	1	16.5	-
SG07-08[c]	1.8	839	34.7	0.40 ± 0.05	1459	100	5	34.6	37.3
SG08-05[d]	2.9	846	32.6	0.29 ± 0.04	2025	100	6	32.1	42.1
SJ1605	2.5	656	39.6	0.251 ± 0.023	2381	24	28	37.1	44.9
SJ1604	1.3	608	39.7	0.160 ± 0.014	2509	27	53	36.7	41.5
SJ1603	1.2	620	42.1	0.202 ± 0.019	2765	0	61	39.5	47.7
SJ1601	3.6	548	43.2	0.154 ± 0.014	2409	58	48	39.4	47.8
SJ1602	3.0	557	42.4	0.126 ± 0.011	2462	44	45	39.4	47.1
SJ1701	0.65	401	43.4	0.234 ± 0.023	1956	100	41	38.6	50.4
SJ1702	1.2	465	46.0	0.61 ± 0.09	2138	100	52	42.0	49.9
SJC0804[a]	5.4	713	23.6	0.045 ± 0.004	2458	44	13	23.0	27.4
SJC0805[a]	6.8	678	14.8	0.061 ± 0.005	2655	30	5	14.5	21.5

[1] Larger watersheds indicate catchments used to evaluate nested erosion rates. Large watersheds have no surface cover mapping. Previously published erosion rate data come from: [a] Rossi (2014); [b] DiBiase et al. (2010); [c] DiBiase et al. (2012); [d] Heimsath et al. (2012).

[2] Headwater catchments indicate ^{10}Be sample catchments where surface cover was mapped in detail.

[3] MAP = catchment-averaged mean annual precipitation (http://prism.oregonstate.edu).

[4] Catchment mean hillslope angle in units of degrees. [5] Mean hillslope angle in degrees for regions of catchment mapped as soil.

[6] Mean hillslope angle in degrees for regions of catchment mapped as bedrock. Values are not reported for soil-mantled catchments with <5% bedrock exposed on hillslopes.

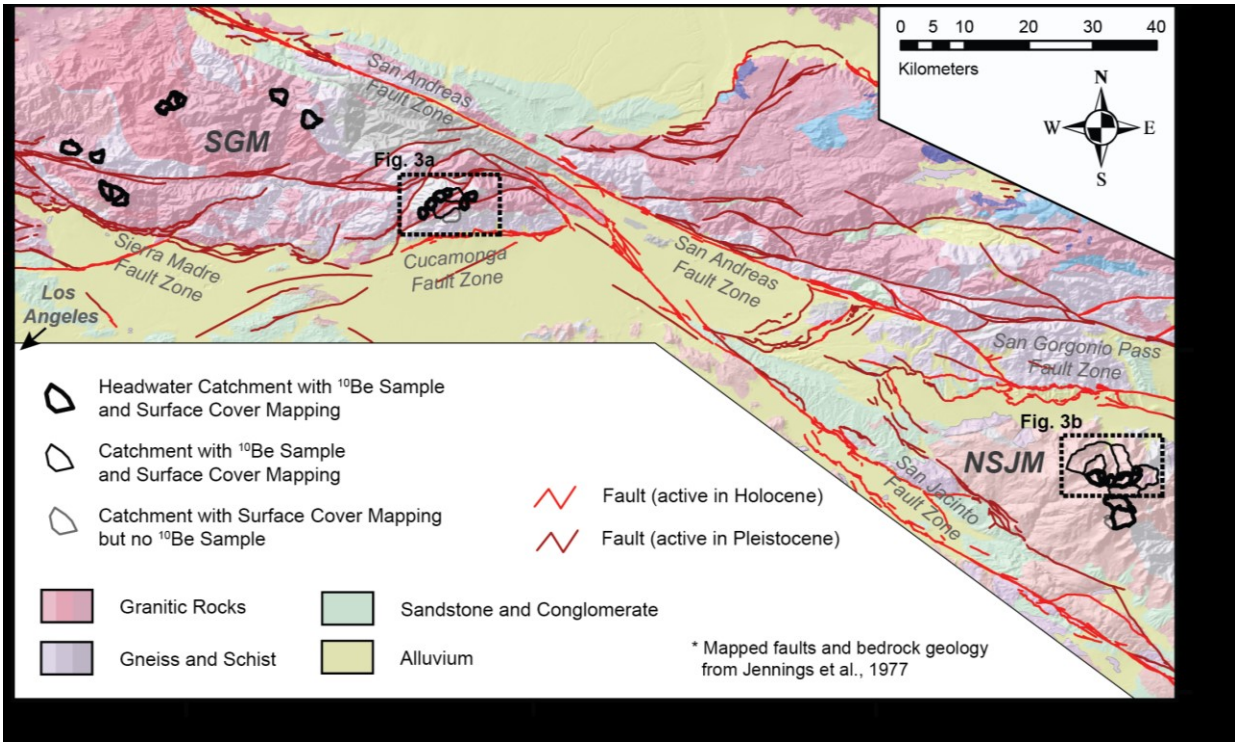

Figure 1. Regional overview map showing bedrock lithology, mapped Quaternary faults, and analyzed watersheds in SGM and NSJM. New ^{10}Be samples were taken within regions enclosed by black-dashed boxes (highlighted in Fig. 3).

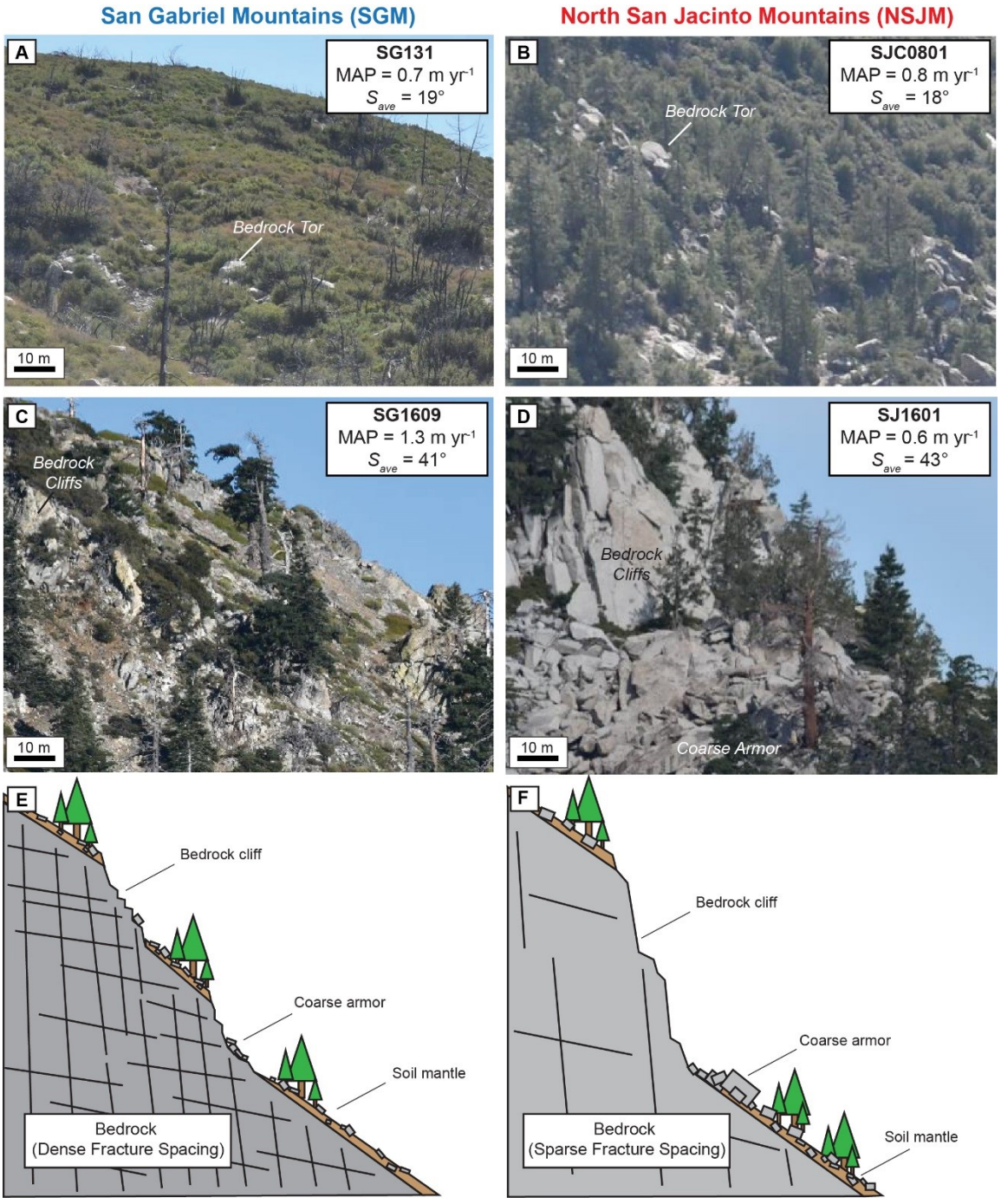

Figure 2. Photographs of hillslopes from San Gabriel Mountains (SGM - A, C) and Northern San Jacinto Mountains (NSJM - B, D) at similar scale. Inset boxes list catchment name, mean annual precipitation (MAP), and catchment-mean hillslope angle, S_{ave}. Cartoons (E, F) show simplified hillslope profiles that highlight contrasting bedrock fracture density, cliff morphology, and clast size of surface cover.

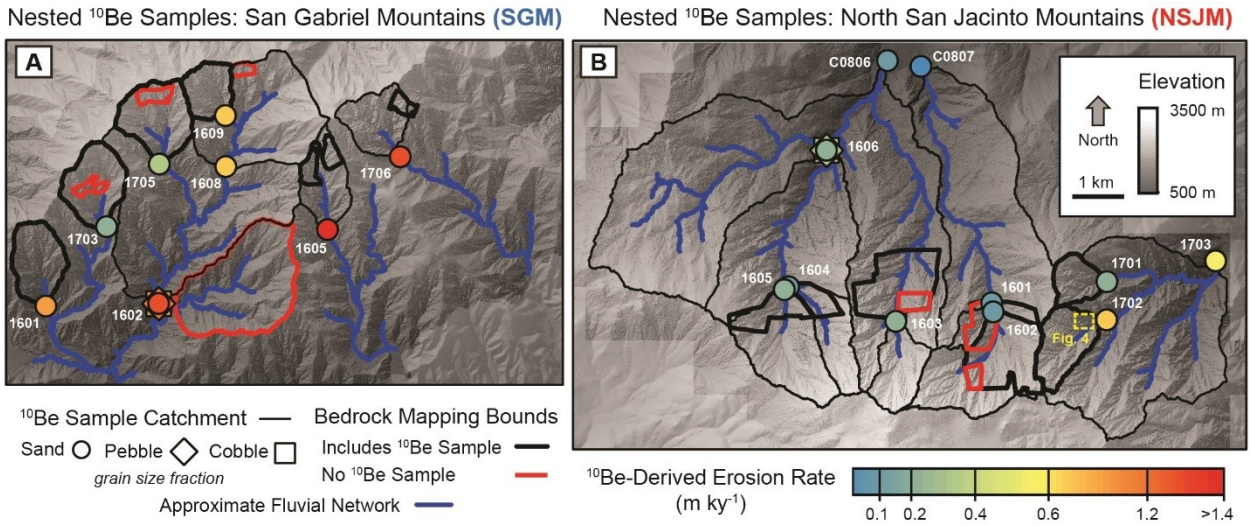

Figure 3. Spatial patterns of erosion rate calculated from new detrital ^{10}Be samples in the SGM (A) and NSJM (B) are shown on top of lidar topography. Catchment outlines show nested basin sampling strategy and white numbers refer to Sample IDs. Sample IDs for SGM samples in (A) are preceded by "SG", and sample IDs for NSJM samples in (B) are preceded by "SJ". Bold black boundaries indicate regions where bedrock was mapped using high-resolution orthophotos. Red boundaries indicate regions where bedrock was mapped and compared to lidar topography, but not associated with a ^{10}Be sample.

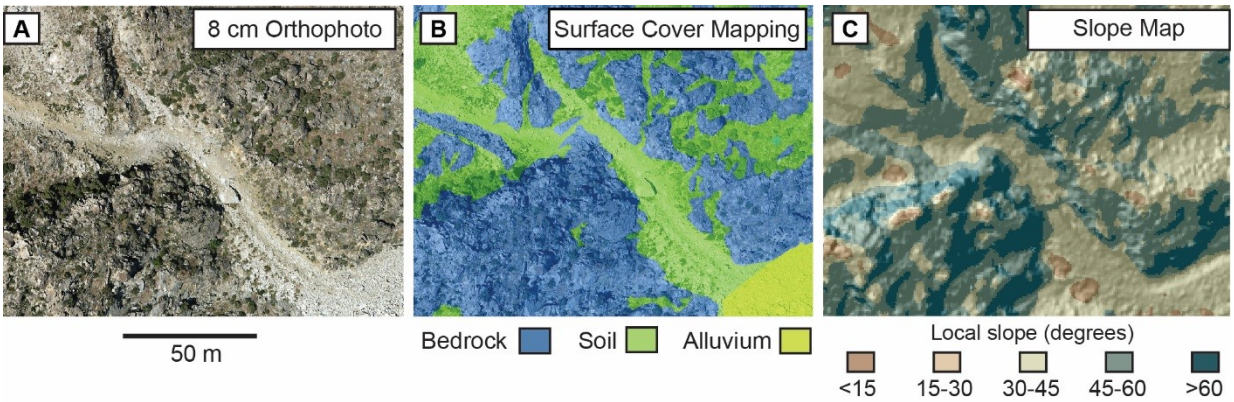

Figure 4. Example orthophoto, bedrock mapping, and slope map for a hillslope with patches of exposed bedrock and soil. Same scale is used for all panels. Extent is highlighted in Fig. 3B.

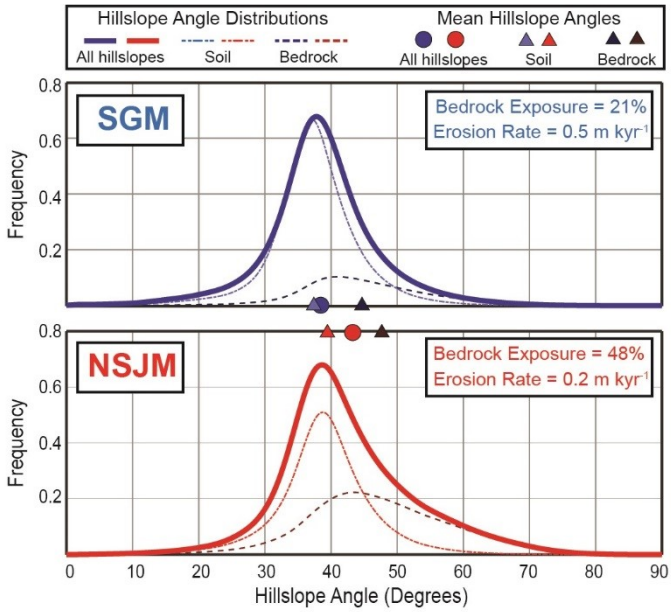

712

713 **Figure 5.** Kernel density function plots of hillslope angles for headwater catchments with mean hillslope angle >35°
714 in the SGM and NSJM. The erosion rates reported on these figures are the erosion rates of each catchment with
715 surface cover mapping weighted by the area of the region where surface cover was mapped (Table 1). Hillslope
716 angle distributions are plotted for all hillslopes, bedrock hillslopes only, and soil-mantled hillslopes only. Means of
717 each distribution are marked with symbols on the x-axis.
718

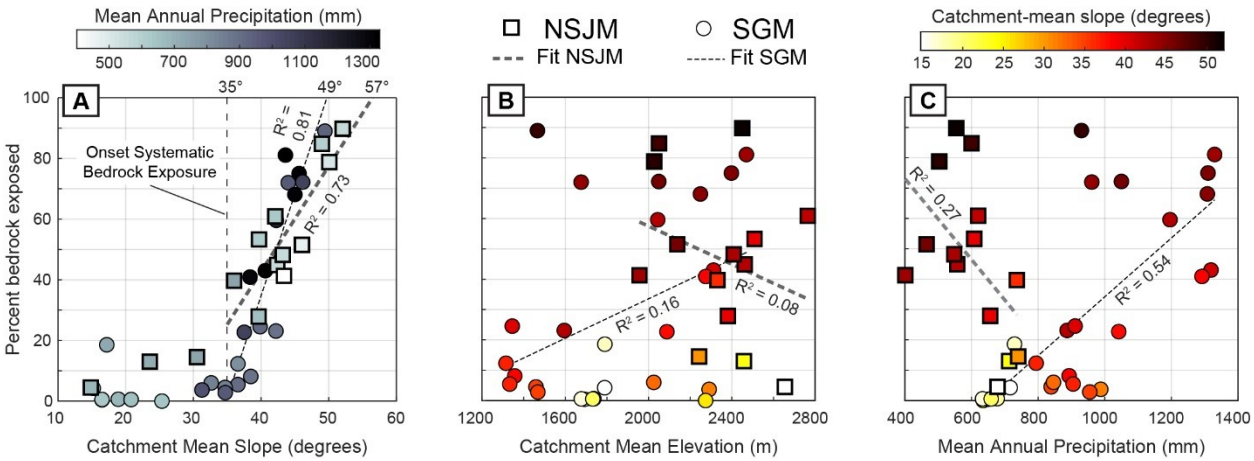

Figure 6. Percent bedrock exposure plotted as a function of catchment-mean hillslope angle, mean elevation, and mean annual precipitation in NSJM (squares) and SGM (circles). Linear regressions for each landscape are marked with dotted lines. (A) Greyscale shading shows mean annual precipitation trends on top of topographic data. (B-C) Shading shows mean catchment slope trends on top of elevation and precipitation data.

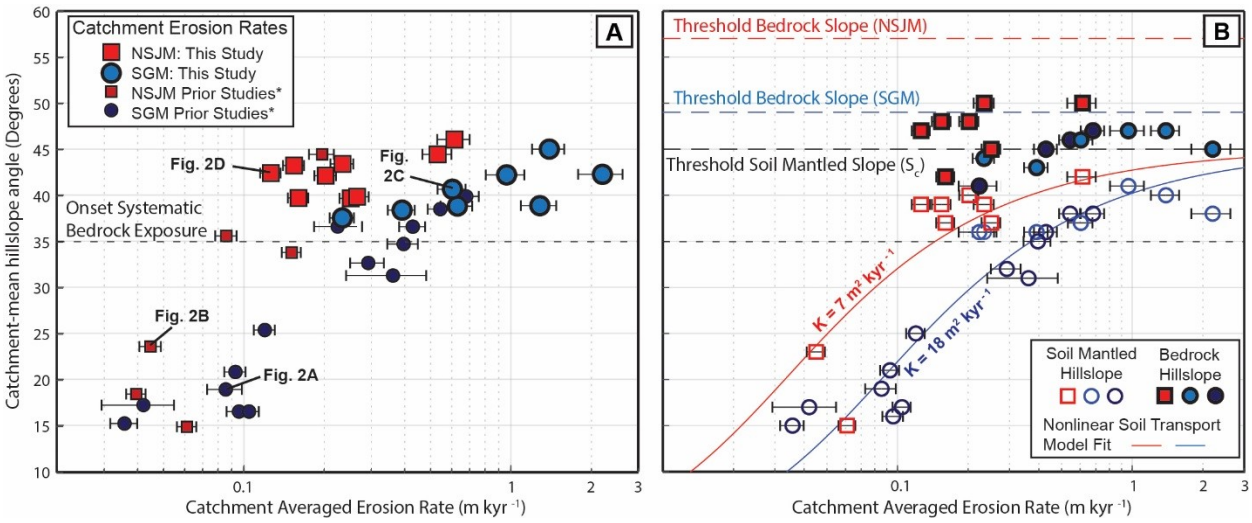

Figure 7. (A) Catchment-mean hillslope angle versus catchment-averaged erosion rates derived from sand-sized fraction detrital in-situ ^{10}Be samples in the NSJM and SGM (Table 1). Annotations denote catchments highlighted by photographs in Figure 2. (B) Same as (A), except plotting mean slope of soil-mantled and bedrock fractions of hillslopes. Solid lines indicate non-linear hillslope transport model fits to soil mantled slopes with contrasting soil transport efficiency, K, between the NSJM and SGM (Roering et al., 2007). Dashed horizontal lines indicate the critical slope of soil, $S_c = 45°$, in the non-linear hillslope transport model (black) and extrapolated threshold mean slopes for bedrock hillslopes (49° and 57°) inferred from Figure 6A (blue and red).

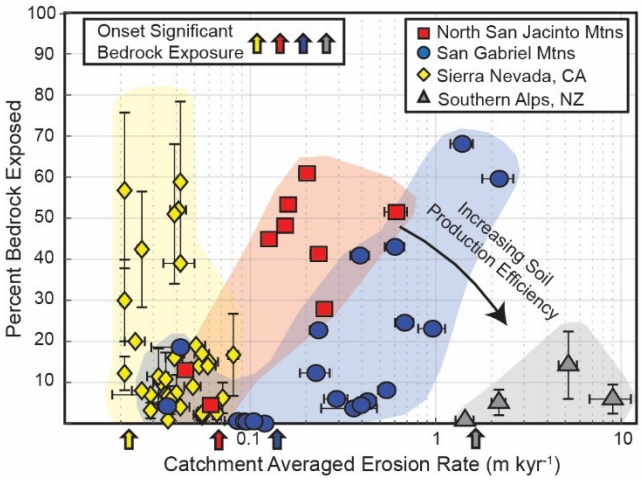

Figure 8. Percent bedrock exposed on hillslope versus catchment-averaged erosion rate, highlighting a wide range of erosion rates where bedrock exposure begins to increase systematically in each landscape (colored arrows below x-axis). The onset of significant bedrock exposure is defined as the erosion rate above which bedrock exposure exceeds a minimum value of 5% and increases systematically with catchment erosion rate (with an exception in the Sierra Nevada Mountains, where bedrock exposure is relatively uncorrelated with erosion rates; see discussion in section 5.2). See supplement for methods of bedrock exposure mapping on satellite imagery and bedrock exposure data from Southern Alps, NZ and Sierra Nevada, CA (Supplementary Table S3).

Bedrock fracture density controls on hillslope erodibility in steep, rocky landscapes with patchy soil cover, southern California, USA

Alexander B. Neely[1], Roman A. DiBiase[1, 2], Lee B. Corbett[3], Paul R. Bierman[3], Marc W. Caffee[4,5]

[1]*Department of Geosciences, Pennsylvania State University, University Park, Pennsylvania, USA 16802*

[2]*Earth and Environmental Systems Institute, Pennsylvania State University, University Park, Pennsylvania, USA 16802*

[3]*Department of Geology, University of Vermont, Burlington, Vermont, USA 05405*

[4]*Department of Physics and Astronomy, Purdue University, West Lafayette, Indiana, USA 47907*

[5]*Department of Earth, Atmospheric, and Planetary Sciences, Purdue University, West Lafayette, Indiana, USA 47907*

Contents

Supplementary methods: Additional methodological details.

Supplementary figures:

Figure S1. Influence of window size on slope calculation

Figure S2. Example drainage density and hillslope morphology

Figure S3. Example bedrock mapping between catchments of similar MAP

Figure S4. Example bedrock mapping on orthophotos and satellite imagery

Supplementary tables:

Table S1. Laboratory preparation and accelerator mass spectrometry (AMS) analysis information for ^{10}Be samples.

Table S2. Topographic data for bedrock mapping regions with no ^{10}Be Sample

Table S3. Erosion rate and bedrock mapping data for Sierra Nevada, CA, and Southern Alps, NZ

Table S4. Erosion rate and sample location information for samples from prior studies in the SGM and NSJM

Supplementary methods

Influence of window size (DEM resolution) on slope calculation

We assessed DEM quality and slope measurement scale by comparing hillslope morphology of 3 representative hillslope patches in Cucamonga Creek where two lidar DEMs (2013 and 2015) with different point density and vegetation filtering have overlapping coverage. We chose a patch of steep bedrock cliffs, planar hillslopes covered by dense bushes and chaparral, and a small catchment with both types of hillslope. Due to differing point densities during lidar collection, stricter vegetation filtering was applied to the 2013 San Bernardino County lidar (*USGS, SanBernardinoCo-AreaA 2013, published 2018*) point cloud than the 2015 NCALM (*National Center for Airborne Laser Mapping*) lidar point cloud used for this study. We progressively increased the spherical window diameter from 4–60 m for the local slope calculation in CloudCompare and calculated hillslope angle kernel density distributions from the resulting values. For each representative patch, we identified when hillslope angle distributions match between the two DEMs, and we recorded the change in mean hillslope angle that occurs from increasing the window diameter on the local slope calculation. Hillslope angle distributions are different between the two DEMs due to differences in the expression of vegetation-derived noise that is recorded in local slope calculations using a small (4 m) window diameter; however, hillslope angle distributions are nearly identical after increasing the window diameter to 15 m and mean hillslope angle only decreases slightly (1–1.5°) on bedrock cliff hillslopes (Supplementary Fig. S1).

Bedrock mapping using satellite imagery (Fig. 8)

To construct Figure 8, 0.5-m resolution satellite imagery from ArcGIS 10.2 world-imagery (DigitalGlobe, 2014, 2017) was used to map bedrock exposure across small headwater

812 catchments from the New Zealand Southern Alps (Larsen et al., 2014) and Sierra Nevada
813 Mountains of California (Hahm et al., 2014). Bedrock exposure data was directly reported in
814 Granger et al., (2001). Compared to low-altitude imagery and field surveys used in the NSJM
815 and SGM, the available satellite imagery is coarser with poorer quality georeferencing, and
816 bedrock mapping accuracy varies accordingly. We used available imagery to estimate the
817 fraction of bedrock exposure, but we do not use bedrock exposure mapping in these catchments
818 to index and separately analyze the morphology of rock and soil mantled hillslopes. We
819 estimated bedrock exposure by mapping the extent of non-vegetated hillslopes and assigning a
820 range of possible bedrock exposure (error bars, Fig. 8, Supplementary Figure S4). For the New
821 Zealand Southern Alps, we conservatively estimated 25% to 100% bedrock exposure within non-
822 vegetated hillslope patches; for catchments in the Sierra Nevada (Hahm et al., 2014), imagery is
823 higher quality and bedrock exposure is easier to identify so we estimated a range of 50% to
824 100% bedrock exposure for unvegetated regions.

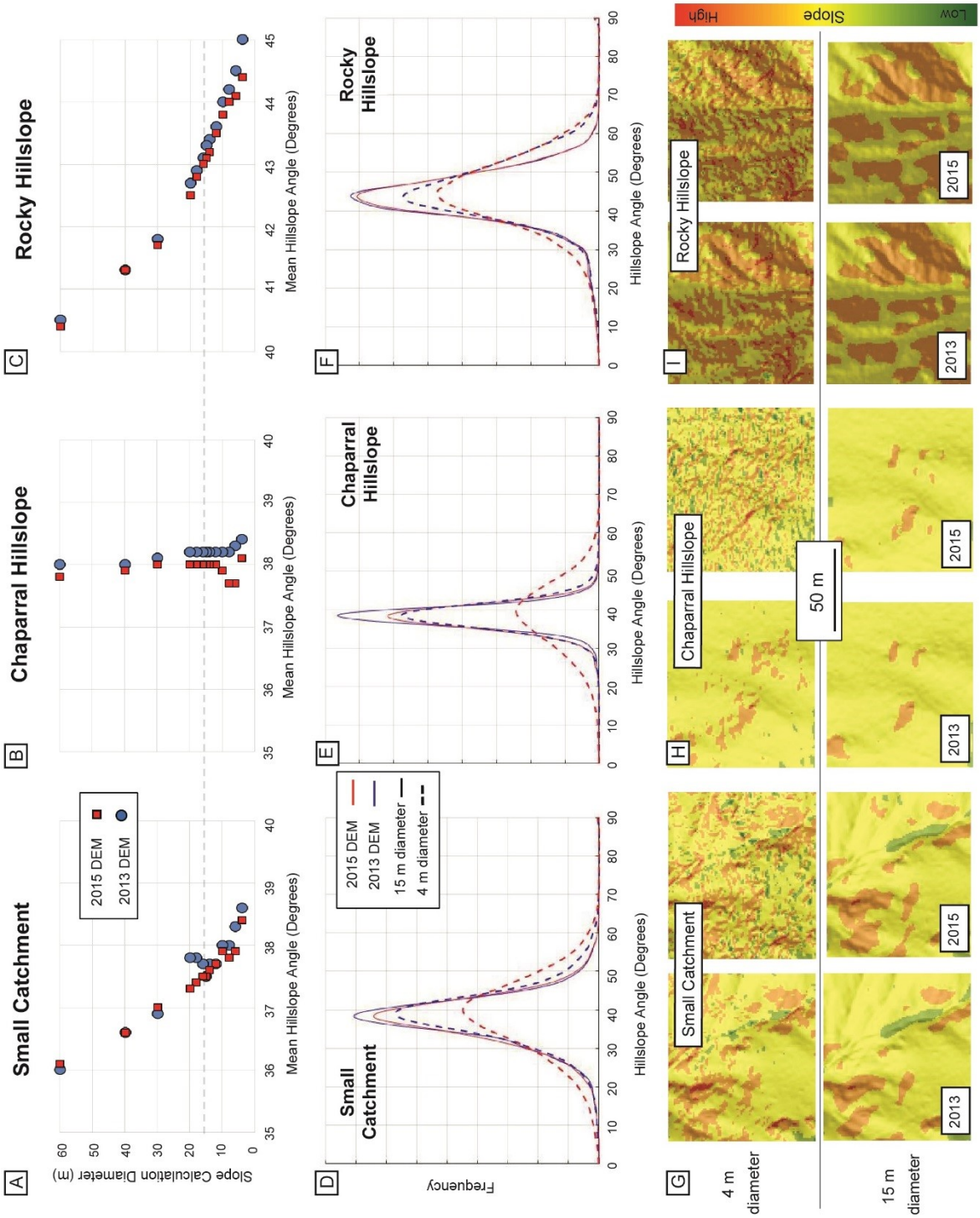

Figure S1. Effect of slope measurement scale on hillslope angle distributions for small catchment, chaparral hillslope, and rocky hillslope. (A-C) Mean hillslope angle changes in example hillslopes as a function of increasing window diameter used to calculate local slope (Red = 2015 DEM, Blue = 2013 DEM). (D-F) Changes in hillslope angle distributions between both DEMs for each example hillslope. (G-I) Slope maps using a window diameter of 4 m and 15 m for example patch within each region on 2013 and 2015 DEMs (same scales).

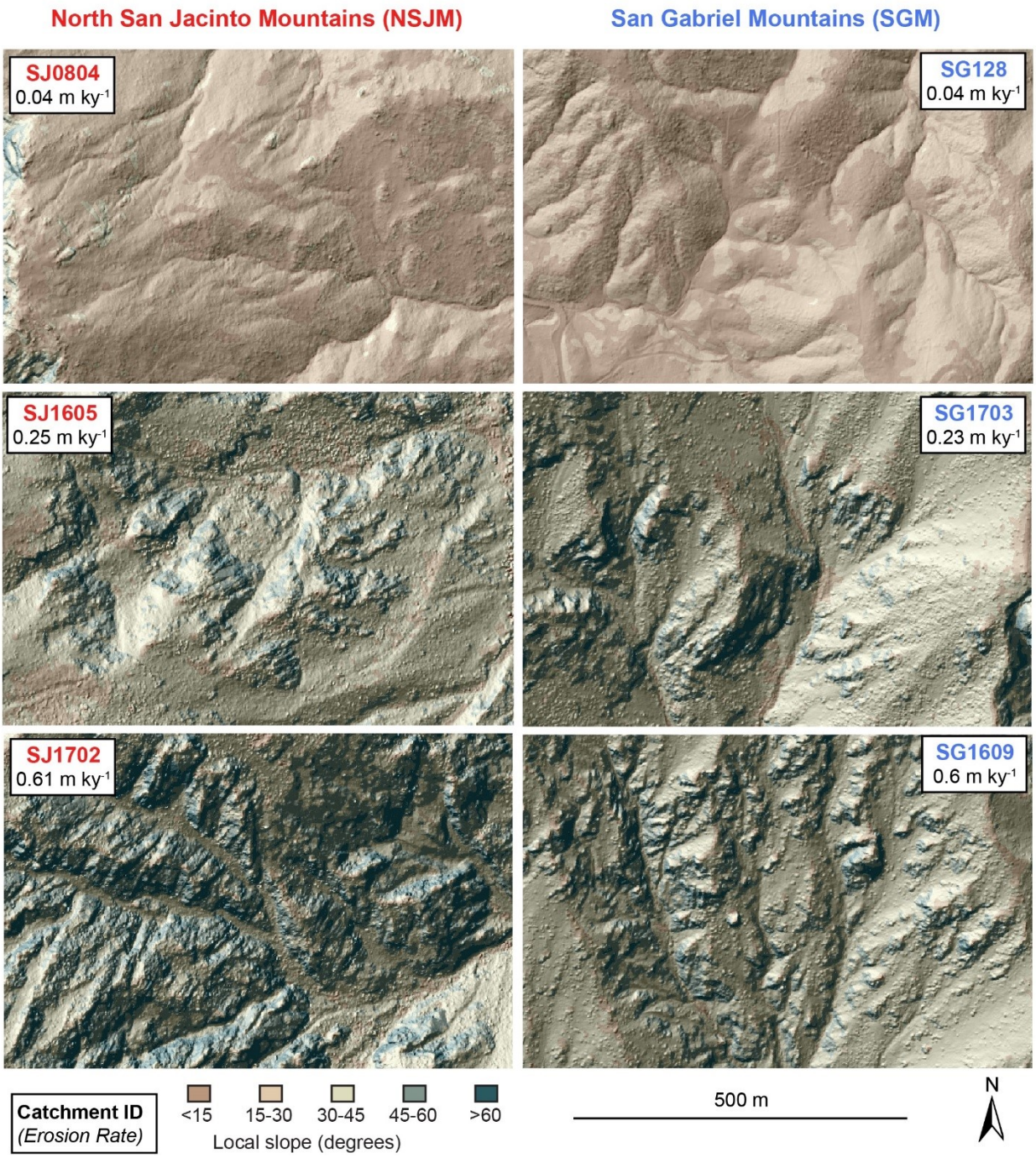

Figure S2. Slopeshade maps showing qualitative hillslope morphology and drainage density in NJSM (left) and SGM (right) as catchment erosion rates increase (top to bottom). Qualitatively, we see no systematic spatial patterns in bedrock cliff exposure (hillslope angles typically >45°) with hillslope position.

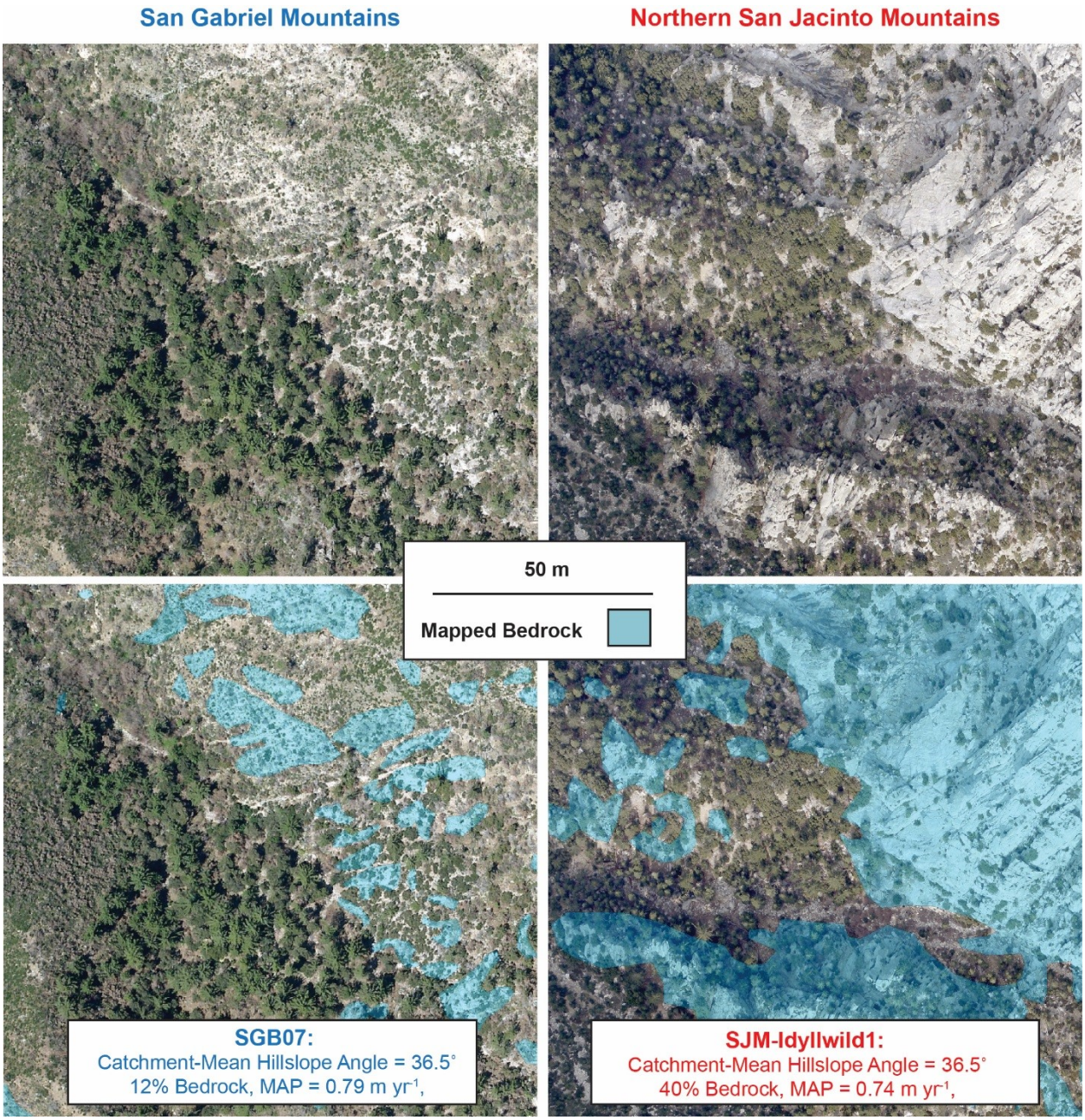

Figure S3. 15 cm resolution orthophotos show bedrock mapping for SGM catchment (left) and NSJM catchment (right). Bedrock is shaded blue. Two SGM and NSJM catchments have similar mean annual precipitation and mean slope, but ~3x more bedrock is exposed on NSJM hillslopes than SGM hillslopes.

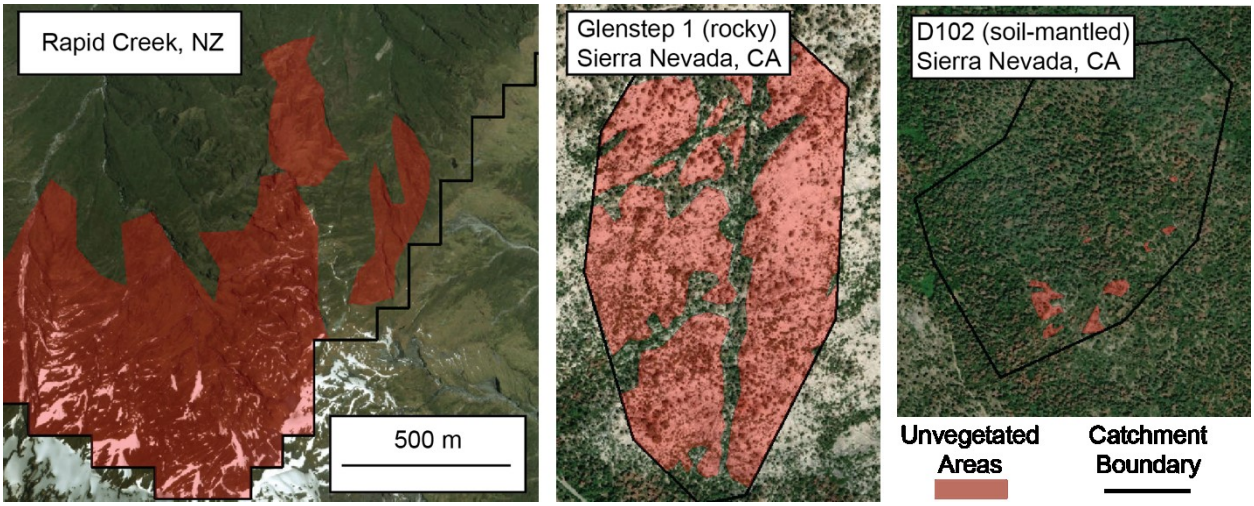

Figure S4: Panels show example bedrock estimation from satellite photographs of headwater catchments in the Southern Alps, New Zealand (left) and Sierra Nevada Mountains, CA (middle, right). Red shading indicates regions mapped as 25 – 100 % exposed bedrock (Fig. 8 vertical error bars), scale bar applies to all panels.

Table S1. Laboratory preparation and accelerator mass spectrometry (AMS) analysis information for ^{10}Be samples.

Sample ID	Latitude	Longitude	Drainage area (km^2)	Size fraction[1]	Quartz mass (g)	^{9}Be added (µg)	Be cathode number[2]	Measured ^{10}Be/^{9}Be (x 10^{-15})[3]	^{10}Be concentration (x 10^3 atoms g^{-1})	Effective elevation (m)[4]	Catchment Erosion Rate (m kyr^{-1})[5]
SG1601	34.1906	-117.6434	1.2	Sand	22.270	240.0	144615	11.8 ± 1.7	8.5 ± 1.2	1614	0.96 ± 0.16
SG1602	34.1910	-117.6216	12.4	Sand	21.966	242.3	144616	10.7 ± 1.4	7.9 ± 1.0	1944	1.28 ± 0.19
SG1603	34.1910	-117.6216	12.4	Pebble	19.019	242.2	150336	10.1 ± 1.3	8.6 ± 1.1	1944	1.2 ± 0.18
SG1604	34.1910	-117.6216	12.4	Cobble	19.904	241.9	150337	13.2 ± 1.6	10.7 ± 1.3	1944	0.95 ± 0.14
SG1605	34.2036	-117.5867	1.2	Sand	21.867	241.5	144617	6.7 ± 1.1	4.9 ± 0.8	2060	2.2 ± 0.4
SG1608	34.2140	-117.6075	4.3	Sand	18.088	241.6	144618	20.9 ± 2.3	18.7 ± 2.0	2191	0.63 ± 0.09
SG1609	34.2226	-117.6076	0.8	Sand	19.773	241.7	144619	25.8 ± 2.3	21.1 ± 1.9	2317	0.60 ± 0.07
SG1703	34.2038	-117.6311	1.3	Sand	21.381	239.6	150358	63.5 ± 4.3	47.5 ± 3.2	2098	0.234 ± 0.024
SG1705	34.2142	-117.6206	1.9	Sand	12.016	241.9	150338	23.7 ± 2.0	31.9 ± 2.7	2285	0.39 ± 0.05
SG1706	34.2159	-117.5721	1.2	Sand	19.931	240.8	150339	10.1 ± 1.2	8.9 ± 1.0	2268	1.39 ± 0.19
SJ1601	33.8329	-116.6589	3.6	Sand	21.958	241.6	144620	118.6 ± 4.9	87.2 ± 3.6	2434	0.154 ± 0.014
SJ1602	33.8311	-116.6584	3.0	Sand	22.179	241.4	144622	150.8 ± 5.4	109.7 ± 3.9	2477	0.126 ± 0.011
SJ1603	33.8296	-116.6784	1.2	Sand	22.052	241.0	144623	111.8 ± 5.1	81.7 ± 3.7	2782	0.202 ± 0.019
SJ1604	33.8357	-116.6997	1.3	Sand	22.171	241.8	144624	122.4 ± 4.4	89.2 ± 3.2	2530	0.160 ± 0.014
SJ1605	33.8350	-116.7005	2.5	Sand	17.945	241.9	144625	58.6 ± 2.8	52.8 ± 2.5	2402	0.251 ± 0.023
SJ1606	33.8586	-116.6920	9.0	Sand	14.063	240.6	144626	36.2 ± 2.5	41.4 ± 2.9	2098	0.27 ± 0.03
SJ1607	33.8586	-116.6920	9.0	Pebble	18.113	241.1	150341	33.8 ± 2.2	30.0 ± 1.9	2098	0.37 ± 0.04
SJ1608	33.8586	-116.6920	9.0	Cobble	19.940	240.5	150342	44.8 ± 2.5	36.1 ± 2.0	2098	0.30 ± 0.03
SJ1701	33.8365	-116.6357	0.7	Sand	19.996	241.1	150343	53.7 ± 3.2	43.3 ± 2.6	1964	0.234 ± 0.023
SJ1702	33.8298	-116.6354	1.2	Sand	20.015	241.3	150344	20.6 ± 2.0	16.6 ± 1.6	2150	0.61 ± 0.09
SJ1703	33.8397	-116.6137	9.8	Sand	20.008	240.2	150345	23.2 ± 2.6	18.6 ± 2.1	1743	0.53 ± 0.07

[1] Sand: 250–850 µm (sieved); Pebble: 2–6 cm (sieved); Cobble: 8–12 cm (intermediate axis diameter measured by hand).

[2] Identification for each sample within the database at the Purdue Rare Isotope Measurement Laboratory (PRIME Lab), West Lafayette, Indiana, USA. Cathode numbers with prefix "14" were analyzed 7/24/17, and ^{10}Be/^{9}Be ratios were reduced using an average of n = 6 process blanks (8.5 ± 5.4 ×10^{-16}, 1SD). Cathode numbers with prefix "15" were analyzed 3/25/18 and ^{10}Be/^{9}Be ratios were reduced using an average of n = 5 process blanks (6.4 ± 1.3 ×10^{-16}, 1SD).

[3] Blank-corrected ratios normalized using ICN standard 07KNSTD3110 with a ratio of 2.85 × 10^{-12} (Nishiizumi et al., 2007). Reported errors indicate 1σ AMS measurement uncertainties and incorporate blank uncertainty.

[4] Effective elevation used for production rate scaling (e.g., Portenga and Bierman, 2011).

[5] Erosion rates calculated using CRONUS calculator (Balco et al., 2008) wrapper script version 2.3, time independent production scaling (Lal, 1991; Stone, 2000), muon production according to Balco (2017), ^{10}Be half-life according to (Nishiizumi et al., 2007), assuming rock density of 2.7 g cm^{-3}.

863 **Table S2.** Topographic Data of Regions with no detrital in-situ ^{10}Be sample[1].

Region ID	Area (km^2)	Mean elevation (m)	MAP (mm yr^{-1})[2]	Mean hillslope angle (degrees)	% Bedrock exposure
SG127-Cliffs1	0.04	1466	930	49.4	89
SG127-Cliffs2	0.06	1676	961	44.0	72
SG1602-Trib	3.37	1468	955	34.7	3
SG1608-Cliffs	0.09	2398	1310	45.6	75
SG1703-Cliffs	0.10	2049	1050	46.2	72
SG1705-Cliffs	0.15	2470	1330	43.6	81
SJM-Idyllwild1	1.48	2331	736	36.0	40
SJM-Idyllwild2	0.35	2243	740	30.5	15
SJ1601-cliffs1	0.41	2027	503	50.1	79
SJ1601-cliffs2	0.11	2450	554	52.1	90
SJ1603-cliffs	0.18	2050	600	49.0	85

864 [1] See supplemental dataset S1 (GIS shapefiles) for location of mapping regions (Fig. 1, Fig. 3).
865 [2] MAP = Mean annual precipitation averaged over region (http://prism.oregonstate.edu).
866

867 **Table S3.** Erosion rates and bedrock exposure from Sierra Nevada, CA and Southern Alps, NZ.

Catchment Name[1]	Erosion Rate (m kyr^{-1})	Erosion Rate 1-σ Uncertainty (m kyr^{-1})	% Bedrock Exposed on Hillslopes	% Bedrock Exposure Uncertainty
AP-1[a]	0.035	0.003	7	0
AP-2[a]	0.041	0.003	17	0
AP-3[a]	0.053	0.005	14	0
AP-4[a]	0.041	0.004	52	0
AP-5[a]	0.060	0.007	15	0
AP-6[a]	0.051	0.006	19	0
AP-7[a]	0.059	0.006	14	0
AP-9[a]	0.055	0.005	17	0
AP-13[a]	0.042	0.005	4	0
AP-14[a]	0.049	0.005	9	0
AL-3[a]	0.039	0.004	16	0
AL-4[a]	0.024	0.003	20	0
AL-5[a]	0.029	0.011	7	0
AL-6[a]	0.026	0.003	8	0
AL-9[a]	0.042	0.008	39	0
AL-10[a]	0.033	0.003	10	0
Glen Step 1[b]	0.042	0.002	59	20
Glen Step 4[b]	0.026	0.001	42	14
SNS17[b]	0.021	0.001	57	19
SNS30[b]	0.021	0.001	30	10
SNS31[b]	0.021	0.001	12	4
Summit Step[b]	0.039	0.001	51	17
Big Creek 5[b]	0.054	0.005	2	1
D102[b]	0.055	0.002	2	1
Mill Creek 1[b]	0.036	0.002	7	4
Musik Creekb	0.055	0.003	2	1
Nutmeg Creek[b]	0.066	0.004	3	2
P301[b]	0.040	0.001	7	4
P303[b]	0.037	0.001	6	3
P304*[b]	0.032	0.004	11	7
Rush Creek[b]	0.036	0.002	1	1
Saginaw Creek[b]	0.035	0.001	11	7
Summit2[b]	0.071	0.004	6	4
Summit3[b]	0.081	0.005	17	10
Swanson Meadow[b]	0.029	0.001	3	2
Fox[c]	1.44	0.16	1	0
Docherty[c]	2.19	0.19	5	3
Gunn[c]	9.02	2.26	6	4
Rapid[c]	5.19	0.59	14	8

868 [1] Erosion rates are reported directly from [a] Granger et al. (2001); [b]Hahm et al. (2014); [c]Larsen et al. (2014).

869

870 **Table S4.** ^{10}Be and catchment information for samples from prior studies in the SGM and NSJM

Sample ID	Source[1]	Latitude	Longitude	^{10}Be concentration (x 10^3 atoms g^{-1})	Effective Elevation (m)	Catchment Erosion Rate (m kyr^{-1})
SG125	DiBiase et al., (2010)	34.2115	-118.0813	16.1 ± 1.3	1342	0.43 ± 0.05
SG126	DiBiase et al., (2010)	34.2184	-118.0840	13.0 ± 0.9	1371	0.54 ± 0.06
SG127	DiBiase et al., (2010)	34.2185	-118.0853	10.3 ± 0.9	1362	0.68 ± 0.08
SG128	DiBiase et al., (2010)	34.3381	-118.0106	250 ± 21	1793	0.036 ± 0.004
SG129	DiBiase et al., (2010)	34.3404	-118.0121	214 ± 57	1793	0.042 ± 0.013
SG131	DiBiase et al., (2010)	34.3659	-117.9931	103 ± 13	1733	0.085 ± 0.013
SG132	DiBiase et al., (2010)	34.3652	-117.9900	94.5 ± 4.5	1733	0.093 ± 0.009
SG136	DiBiase et al., (2010)	34.3287	-117.7891	103 ± 4.5	2275	0.120 ± 0.011
SG151	DiBiase et al., (2010)	34.3202	-117.8003	34.8 ± 10	2296	0.36 ± 0.12
SG205	DiBiase et al., (2010)	34.3617	-117.9928	89.3 ± 5.8	1693	0.096 ± 0.010
SGB-7	DiBiase et al., (2010)	34.2979	-118.1487	29.2 ± 4.7	1323	0.22 ± 0.04
SG07-01	DiBiase et al., (2010)	34.3646	-117.9930	81.2 ± 3.5	1673	0.104 ± 0.009
SG07-08	DiBiase et al., (2012)	34.2862	-118.0963	18.9 ± 2.0	1467	0.40 ± 0.05
SG08-05	Heimsath et al., (2012)	34.3692	-117.8394	36.7 ± 4.4	2036	0.29 ± 0.04
SJC0801	Rossi (2014)	33.8057	-116.6393	414 ± 8.4	2688	0.040 ± 0.003
SJC0802	Rossi (2014)	33.8397	-116.6137	44.8 ± 3.3	1745	0.196 ± 0.021
SJC0804	Rossi (2014)	33.7795	-116.6467	359 ± 16	2754	0.045 ± 0.004
SJC0805	Rossi (2014)	33.7776	-116.6476	225 ± 4.9	2492	0.061 ± 0.005
SJC0806	Rossi (2014)	33.8739	-116.6803	63.7 ± 1.7	1886	0.151 ± 0.012
SJC0807	Rossi (2014)	33.8726	-116.6737	104 ± 4.9	1775	0.086 ± 0.008

871 [1] See cited references for specific laboratory preparation and accelerator mass spectrometry (AMS) information.
872